TECHNICAL UNIVERSITY OF CRETE
SCHOOL OF ELECTRONIC AND COMPUTER ENGINEERING
TELECOMMUNICATIONS DIVISION



# Scatter Radio Sensor Network
# with Analog Frequency Modulation Principles

by

Eleftherios Kampianakis

A THESIS SUBMITTED IN PARTIAL FULFILLMENT OF
THE REQUIREMENTS FOR THE MASTER OF SCIENCE OF

ELECTRONIC AND COMPUTER ENGINEERING

July 25, 2014

THESIS COMMITTEE

Associate Professor Aggelos Bletsas, *Thesis Supervisor*
Professor Apostolos Dollas
Assistant Professor Eftichios Koutroulis

# Abstract

Scatter radio communication is implemented with very simple, low-power and low-cost front-ends that only consist of a single radio frequency (RF) switch. This work develops a bistatic scatter radio wireless sensor network (WSN) with *analog* energy-assisted tags that monitor relative humidity percentage (%RH) and consume less than 1 mWatt power. Particularly, the tags employ a capacitance-to-frequency converter, that is implemented with a 555 timer and modulates the capacitance of the HCH-1000 %RH sensor. The frequency-modulated pulses are routed to the tag's RF front-end which is designed to increase communication range. In order to convert the output frequency of the tags to %RH, a transfer function is estimated using careful polynomial surface fitting calibration and including the ambient temperature. Frequency division multiple access (FDMA) networking is implemented with the utilization of different passive components on each tag. Moreover the receiver that is implemented on a software defined radio (SDR) platform exploits carefully designed software filters based on histogram and Savitsky-Golay smoothing techniques. The achieved communication range is over 130 meters at an end-to-end root mean squared error (RMSE) of less than 5 %RH. For the network evaluation, a testbed is calibrated and deployed in a tomato greenhouse demonstrating a novel *analog* bistatic scatter radio WSN. Finally, an over the air programmable (OTAP) testbed was developed, employing nodes that utilize both an active radio front-end and scatter radio front-end in order to facilitate remote monitoring and debugging.

Thesis Supervisor: Associate Professor Aggelos Bletsas

*To my family.*

# Table of Contents

# List of Figures

# List of Tables

# Chapter 1

# Introduction

## 1.1 Motivation

Modern telecommunications have revolutionized the way people interact with and monitor the environment. This revolution is exemplified through the emerging technology of wireless sensor networks (WSNs). Classic WSNs consist of a large number of nodes with capability of forming a network in order to transfer monitored data to a base station. The nodes typically employ a Marconi-type radio that is controlled via a microcontroller unit (MCU). The latter collects data from the environment through and/or interacts with it. This technology has attracted tremendous academic and industrial attention and has been utilized in applications including environmental sensing, wearable biometric monitoring and structural monitoring [1–3]. Moreover, a lot of research has been conducted regarding the exploitation of WSNs in ultra large scale deployments such as the work in [4–7].

However, actual deployments of real-world, large-scale WSNs are rare. Such is the work in [8] where a network of 1196 nodes monitoring $CO_2$ levels is demonstrated. However, as authors mention, the batteries had to be replaced more than once per year (same authors describe the scale-vs-lifetime tradeoff [9]) and the overall cost of the setup is high, since each node costs approximately 36 € [9]. In addition to monetary and lifetime constraints WSN scalability is also constrained by software complexity, as the authors of [10] have indicated. In order to address such constraints, scatter radio has recently started to be exploited for wireless sensing and particularly for the development of WSNs.

## 1.2 Scatter Radio Communication

Scatter radio communication is a concept that emerged in 1948 [11] and is largely exploited today in the well-known radio frequency identification (RFID) tags. RFID tags are ultra low-cost devices that are mainly utilized in object identification (e.g., in supply chains).

Scatter radio communication is implemented with a single switch that alternatively terminates the tag/sensor antenna between two (or more [12]) loads (Fig. 1.1). The antenna S11 parameter (i.e., reflection coefficient $\Gamma$), associated with each antenna terminating load, is modified when the antenna load is changed. Therefore, the amplitude and phase of the carrier signal induced at the sensor/tag[1] antenna is modulated and reflected back to the receiver. As a result, when a continuous wave (CW) with frequency $F_c$ is incident on an antenna that its loads are terminated with a rate $F_{sw}$, two subcarriers emerge in the frequency spectrum, with frequencies $F_c \pm F_{sw}$ [13] (as in Fig 1.1).

The RF front-end of the devices that utilize scatter radio communication can be implemented with very small amount of components (single switch and antenna). Therefore, complexity and cost constraints that are inherent in active-radio WSNs are avoided. As a result, the exploitation of scatter radio-enabled tags in WSNs facilitates the development of large-scale setups. Recent examples that demonstrated the capability of scatter radio for the development of low-cost sensors includes [14, 15].

The classic scatter radio setup is composed of battery-less devices (e.g., RFID tags) that are set up in monostatic topology (i.e., reader in the same box as the carrier emitter) and communicate via high bitrate schemes. Particularly, since the tags do not employ a power source, the electronics that implement sensing and modulation have to be powered up by absorbing the power of the carrier that is incident on the antenna. As a result, the tags require a strong carrier which is available only within a small distance from the carrier emitter [16]. Moreover, the monostatic topology introduces roundtrip

---

[1]In line with standard RFID terminology, the terms "tag" and "sensor" will be used interchangeably.
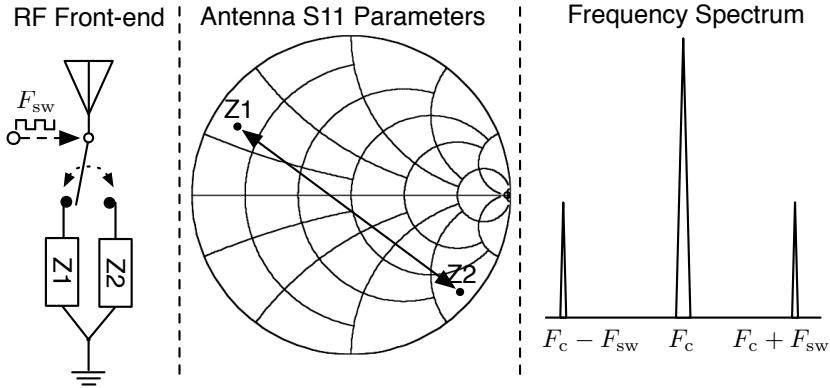
Figure 1.1: Scatter radio communication principles: RF switch alternates the loads of the tag antenna with frequency $F_{sw}$. When a carrier is imminent with frequency $F_c$, two subcarriers appear, with frequencies $F_c \pm F_{sw}$.

path losses that further reduce the communication range. Finally, bitrates that are utilized by commercial RFID systems are on the order of hundreds of kbps. This results in reduced energy per bit, due to the small bit duration, and in decreased signal to noise ratio (SNR). These characteristics reduce the communication range of such communication systems significantly, down to a few meters.

However, the development of a WSN with scatter radio principles requires sensor/tags that can communicate with the reader at distances on the order of at least 100 meters. Recent literature has shown great effort towards improving the communication range by modifying different parts of the system. As an example, works in [17,18] focus on the RF parameters of the tag that affect the communication performance, such as the load selection and the antenna matching. Moreover, work in [19] exploited the utilization of multiple antennas for the improvement of link performances in scatter radio system operating at 5.8 GHz and demonstrated significant range increase. Despite the fact that significant research has been conducted, communication ranges are still on the order of a few meters and the utilization of such setups in long-range WSNs is practically useless.
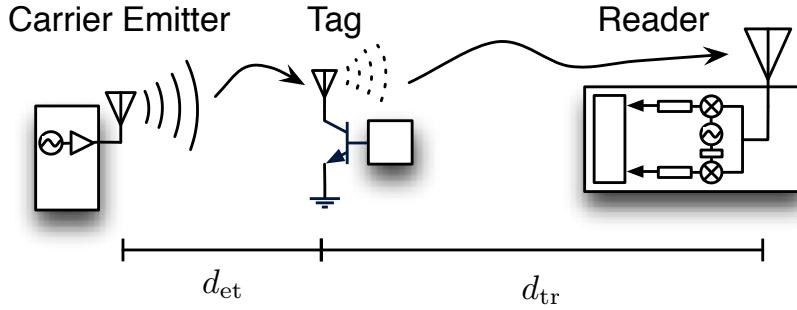
Figure 1.2: Bistatic scatter radio topology; carrier emitter placed in a different location from the reader. $d_{\mathrm{et}}$ and $d_{\mathrm{tr}}$ denote the emitter-to-tag and tag-to-reader distance, respectively.

## 1.3 Scatter Radio Networking and %RH Sensing

In order to address the small communication range problem, systems emerged, that utilize bistatic topology (where the carrier emitter is placed in a different location from the reader), low bitrate and semi-passive (i.e., battery-assisted) tags. Particularly, with the utilization of the bistatic topology, illustrated in Fig. 1.2, the roundtrip path losses can be reduced, and more than one low-cost emitters can illuminate the tags, since the probability of a short distance between emitter and tag is relatively high [20–22].

Additionally, employing low bitrate can increase the sensitivity of the receiver (reader) [13] and this is not an issue with environmental monitoring WSNs, since environmental variables such as relative humidity (%RH) and temperature change with a slow rate. Finally, in order to fully exploit the CW energy for communication purposes, instead of using an amount of it to power up the tag's electronics, tags can be equipped with batteries or other power sources (e.g., solar panels) [13].

All the aforementioned techniques were utilized in [22] where the authors demonstrated a bit-error-rate (BER) on the order of 2%, for a tag-to-reader ($d_{\mathrm{tr}}$) and emitter-to-tag ($d_{\mathrm{et}}$) distances of over 134 m and 4 m respectively. Particularly, the authors of [22] developed a digital tag that communicated using digital frequency-shift keying (FSK) modulation, low-cost carrier emit-
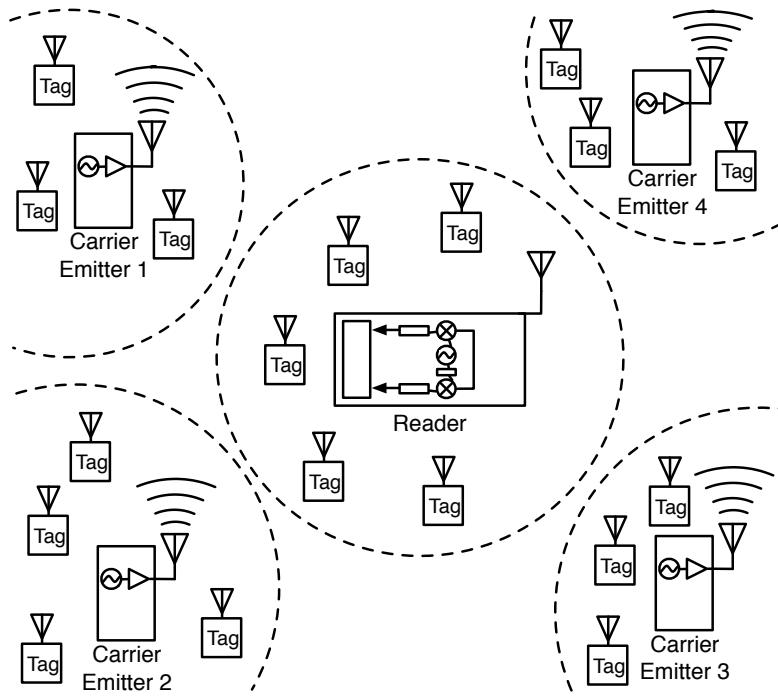
Figure 1.3: Proposed WSN architecture. Multiple, low-cost carrier emitters are placed in the field. Around them many ultra low-power tags are deployed.

ters that emitted a CW at 13 dBm power and utilized a commodity software-defined receiver for the detection of the scattered signals. Finally, works in [14, 15] demonstrated the potential of scatter radio for wireless sensor networking.

With the utilization of the bistatic topology and semi-passive tags that communicate with low bitrate, it is possible to implement large-scale networks, comprising of low-cost sensor/tags. The concept is illustrated in Fig. 1.3: multiple carrier emitters placed around a central emitter and around them, multiple low-power and low-cost tags are spread. Carrier emitters can be fairly simple devices that comprise of an oscillator and a power amplifier while the reader can be implemented in a commodity software defined radio device.

One of the important environmental variables that needs careful monitoring in precision agriculture, is relative humidity (%RH). Relative humidity is one of the major factors that promotes the growth of various bacteria such

as Botrytis [23] and also, high levels of %RH can decrease the mineral intake of plants, leading in a decreased growth and production [24]. There is extensive prior art regarding low-power %RH sensors like for example the works in [25, 26]. The latter however, do not utilize a wireless interface for transfering %RH data. Some examples of passive wireless sensors have also been demonstrated in the past, including works in [27, 28], where inductive coupling techniques are used for the wireless transmission. However, such techniques are inherently limited to short communication ranges of less than a meter. Apart from that, active-transmitter WSNs have been extensively used for environmental monitoring and examples are the works in [29–31]. However, these systems are subject to the constraints that were analyzed previously.

This work describes the development of a scatter radio WSN which utilizes battery-assisted tags set up in bistatic topology. The tags scatter %RH values using analog, frequency modulation (FM) at ranges on the order of 130 meters. This manuscript describes the proposed WSN system, including testbeds and real-world applications that were developed, deployed and evaluated.

# Chapter 2

# Scatter Radio Tags

## 2.1 Analog Frequency Modulators
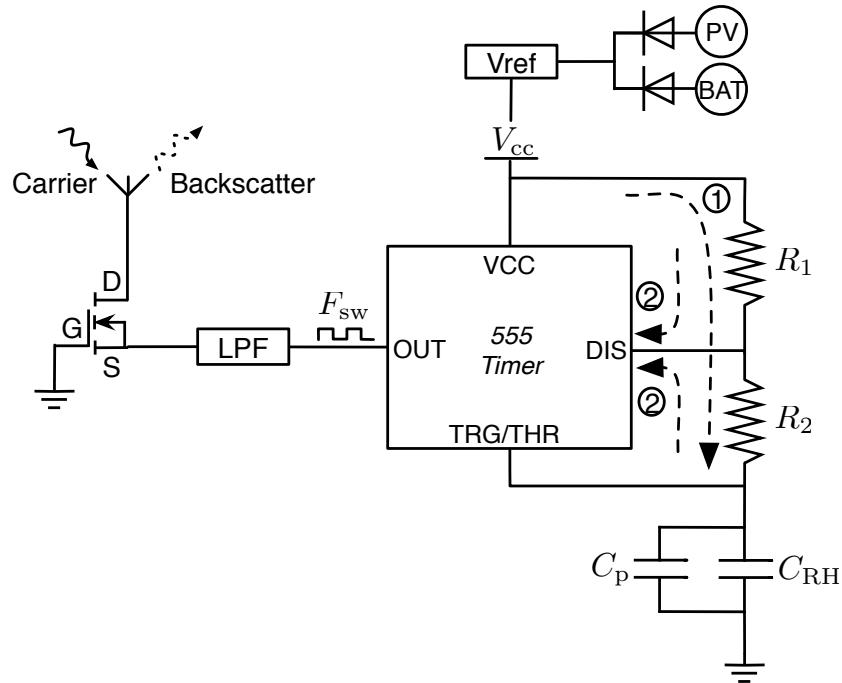


Figure 2.1: Sensor circuit diagram with scatter radio: capacitance varies the timer output frequency, producing a variable-frequency pulse that switches a single transistor; the latter is directly connected to the antenna [32, 33].

The tags that were developed for the proposed WSN are low-power, low-complexity and low-cost, analog devices. The purpose of the sensor/tags is to produce voltage pulses of frequency that depends on the %RH value and use these pulses to control the rate with which the antenna termination loads are alternated. For this purpose, circuit diagram of Fig. 2.1 was designed, that mainly consists of capacitance-to-frequency converter, an RF switch and an

antenna [32, 33].

A 555 timer (Intersil 7555) that is set up in astable multivibrator mode plays the role of the capacitance-to-frequency converter. There are four pins that play a critical part in the timer's operation in this mode: "trigger" (TRG), "threshold" (THR), "discharge" (DIS) and "out" (OUT). Voltage of Pin OUT is controlled by pins TRG and THR, which are short-circuited in astable multivibrator configuration. When voltage at THR is below $V_{cc}/3$, OUT is set to "high" (i.e $V_{cc}$) and DIS is set to high impedance. This state persists until voltage in TRG becomes higher than $2V_{cc}/3$. Then, OUT is set to "low" (i.e $\sim 0$ Volts) and DIS is set to open collector mode (i.e draining current). The timer is connected to a resistor-capacitor (RC) network that contains the Honeywell HCH1000 capacitive %RH sensor (i.e. $C_{RH}$ in Fig. 2.1). Finally, the fabricated tag is depicted in Fig. 2.2 and as one can observe it is fairly small in size, with dimensions 40x28 mm.
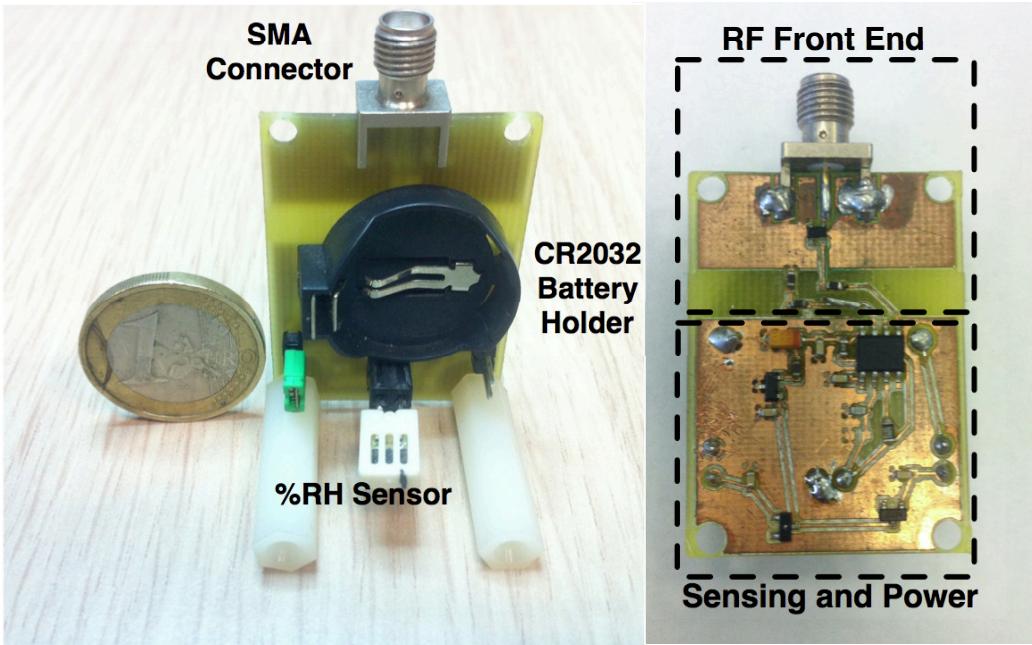


Figure 2.2: The developed prototype sensor tag. The sensing/power part are distinguishable from the RF front-end part.

The RH sensing capacitor is periodically charged and discharged through resistors $R_1$ and $R_2$ (Fig. 2.1). Thus the frequency $F$ and duty cycle $D$ of the

square wave produced at the output of the astable multivibrator are given
by:

$$F = \frac{1}{(R_1 + 2R_2)C\ln(2)},$$  (2.1)

$$D = \frac{R_1 + R_2}{R_1 + 2R_2}.$$  (2.2)

It is noted that $D$ is always over 50 % since $R1 > 0$. The voltage pulses that
are produced by the timer are driven to the RF switch and, as described
in Section 1.2, subcarrier (i.e., switching) frequencies are produced when a
CW is incident on the antenna. Frequency modulation (FM) of the %RH
is implemented, since the value of the subcarrier frequency depends on the
value of %RH. In order to adjust the total capacitance range of the sensor
tag, capacitor $C_p$ is connected in parallel with the sensing capacitor. Thus,
the total capacitance $C$ is given by:

$$C = C_p + C_{RH}.$$  (2.3)

## 2.2 RF Front-End

### 2.2.1 Overview

The RF front-end is responsible for the scattering of the CW and therefore
its operation is crucial for the communication efficiency of the semi-passive
tags. It is important to note that the RF front-end specifications between
semi-passive and passive tags are different. Particularly, the passive tags
are developed in order to absorb part of the energy from the CW in order
to power their electronics. However, this specification does not apply on
the semi-passive tags due to the fact that they are powered by an external
power source (e.g., battery) and the main purpose of their RF-front end is
to maximize scatter radio performance.

For the switching between two different loads in the case of the semi-
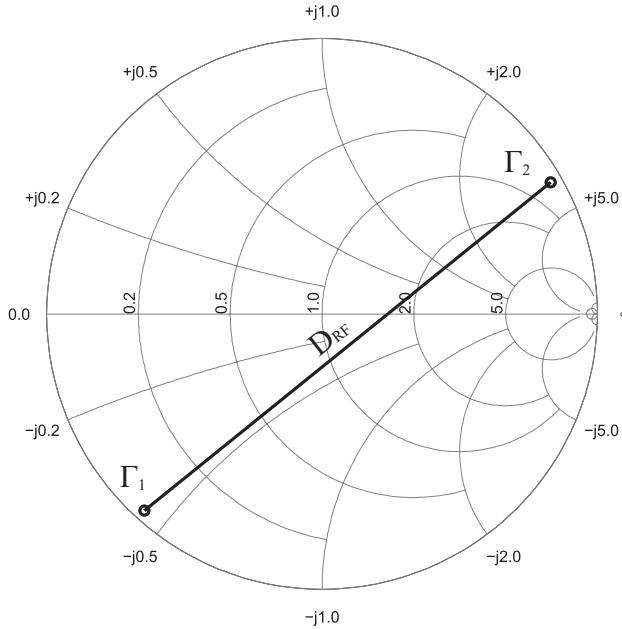
Figure 2.3: $\Gamma_i$s on the Smith chart.

passive tags, a single transistor is usually selected in order to minimize the cost. The transistor operates between two states; open circuit and short circuit. For each transistor state $i$, the antenna terminals have a value $Z_i$ and the antenna-tag system has a corresponding reflection coefficient $\Gamma_i$. The latter describes relation of the amplitude of the reflected wave relative to that of the incident wave and it can be depicted on the Smith chart (as in Fig. 2.3). The reflection coefficient $\Gamma_i$ of the tag-antenna system for the $i$-th state of the transistor is given by:

$$\Gamma_i = \frac{Z_i - Z_{\mathrm{a}}^*}{Z_i + Z_{\mathrm{a}}}, \tag{2.4}$$

where $Z_{\mathrm{a}}$ is the tag's antenna impedance. Hence, the amplitude of the complex reflection coefficient difference between the two states, or equivalently between two loads, $Z_1, Z_2$, connected to the antenna is,

$$D_{\mathrm{RF}} = |\Gamma_1 - \Gamma_2| . \tag{2.5}$$

Scatter efficiency is largely dependent on the term $D_{\mathrm{RF}}$ which, in the ideal case, when $\Gamma_i$s are diametrically opposite on the Smith chart, equals to 2. As $D_{\mathrm{RF}}$ increases, scatter performance is improved [18] and therefore it is desired to develop an RF front-end that amounts for a value of $D_{\mathrm{RF}}$ that is as close to 2 as possible. However, due to losses and phase that is introduced by the non-idealities of the transistor and the PCB layout, $D_{\mathrm{RF}} = 2$ is not easily achieved.

### 2.2.2 RF front-end analysis/experimentation

For this reason, a methodology was proposed [34] for developing an RF front-end with as large value of $D_{\mathrm{RF}}$ as possible. Particularly, the methodology employs the RF front-end microwave design and analysis, so that the antenna and the tag's control circuit are mutually decoupled. Moreover the methodology offers the maximization of the term $D_{\mathrm{RF}}$ with $Z_{\mathrm{a}}$ as a variable and $Z_i$s fixed as well as the estimation of the antenna $Z_{\mathrm{a}}$ with which the tag antenna should be designed.

Initially, a bow-tie antenna was fabricated with a $Z_{\mathrm{a}} = 40.2416 - 4.6807i$ at a frequency of 868 MHz. In order to examine the influence of the antenna impedance on $D_{\mathrm{RF}}$ and subsequently, the influence on scatter efficiency, the antenna was connected with an SMA connector to 3 identical type of lossy coaxial cables with different lengths. The result is 3 different $Z_{\mathrm{a}}$ cases with exactly the same antenna gain and structural mode [18]. The antenna impedances after measurement were,

$$Z_{\mathrm{a}} = [109.1 + 6.2i \quad 42.80 + 21.8i \quad 27.50 + 16.9i]. \qquad (2.6)$$

Assuming that the transistor works as a perfect RF switch with $Z_1 = \infty$ and $Z_2 = 0$ for the open- and short-circuited case respectively, the $D_{\mathrm{RF}}$ values for each $Z_{\mathrm{a}}$ case were:

$$D_{\mathrm{ideal}} = [1.9968 \quad 1.7821 \quad 1.7040]. \qquad (2.7)$$

However, it is obvious that the transistor is not a perfect RF switch, and as a

result, the actual $Z_1$ and $Z_2$ were measured to be $10 - 91.5i$ and $27.8 + 45i$ Ohm, respectively at a frequency of 868 MHz. Therefore, the real value of the $D_{\mathrm{RF}}$s above are actually:

$$D = [1.4027 \quad 1.2688 \quad 1.0650]. \tag{2.8}$$

Based on the above data, it is shown that $Z_i$s should not be taken into account as ideal and that the term $D_{\mathrm{RF}}$ is strongly influenced by parameter $Z_{\mathrm{a}}$. Moreover, it is noted that there is an antenna with optimal load $Z_{\mathrm{a}}$ that maximizes term $D_{\mathrm{RF}}$ which, in this case it produces $D_{\mathrm{RF}} = 1.57$ which is however far away from the optimal $D_{\mathrm{RF}} = 2$. Therefore, the deviations between the ideal and the real case should be taken into consideration in the design process of the tag RF front-end and, also a better RF front-end microwave design is required in order to optimize $D_{\mathrm{RF}}$.

For the validation/characterization of the RF front-end on the end-to-end scatter radio efficiency, a complete system with a tag, a carrier emitter and a receiver was utilized. For each case, the received amplitude (in dBm) of the received subcarrier frequencies was measured and the results were the following:

$$A(\mathrm{dBm}) = [-46.1547 \quad -51.9010 \quad -53.5390]. \tag{2.9}$$

It is obvious that the best and worst case have a significant difference of 7.35 dB.

### 2.2.3 Enhanced RF front-end

For the purposes of developing an enhanced RF front-end, electromagnetic analysis was conducted, in order to select $Z_i$s such that $\Gamma_i$s are diametrically opposite on the Smith chart. A coplanar waveguide structure was fabricated, with the transistor placed as close as possible to the antenna in order to avoid phase introduction. Moreover the RF front-end and the control circuit were mutually decoupled with the utilization of RF chokes that have a high impedance at UHF, thus acting as low pass filters.

The tag with the enhanced RF front-end is depicted in Fig. 2.4. Exper-
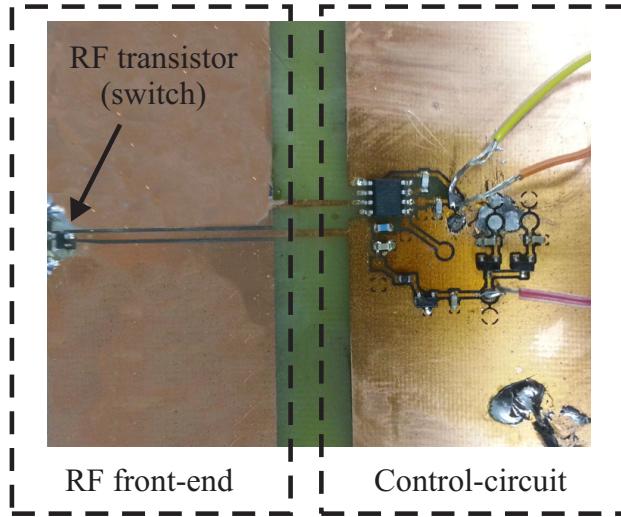
Figure 2.4: Tag with enhanced RF front-end.

imentation with the specific front-end indicated that $Z_1 = 1.3 - 221.2i$ and $Z_2 = 18.1 + 14.4i$, for $-20$ dBm power input at 868 MHz. Subsequently, an antenna load $Z_a$ was found that maximizes $D_{RF}$, based on the measured $Z_1$ and $Z_2$. According to calculations, the antenna load that maximized $D_{RF}$ was $Z_a = 56.6172 + 196.082i$ and for that antenna load, $D_{RF} = 1.916$ (Fig. 2.5) which is a highly improved result compared to the previous 1.57. It is obvious that scatter radio performance is improved in terms of $D_{RF}$ which will in turn lead to improved communication performance. Antenna fabrication with the specific load and real-world experimentation is left for future work.

## 2.3 Multiple Access

The WSN that was developed employs a multiple access control (MAC) scheme that is responsible for the simultaneous communication of multiple tags with the receiver. As described above, the output frequency of the 555 timer, and as a result, the subcarrier frequency, depends on the %RH value. The frequency division multiple access (FDMA) is adopted which works in a way that every tag is assigned a distinct frequency band for operation, in order to avoid collision [13], [35]. Fig. 2.6 illustrates the concept, where one can observe that each tag is allocated a specific frequency band and, also,
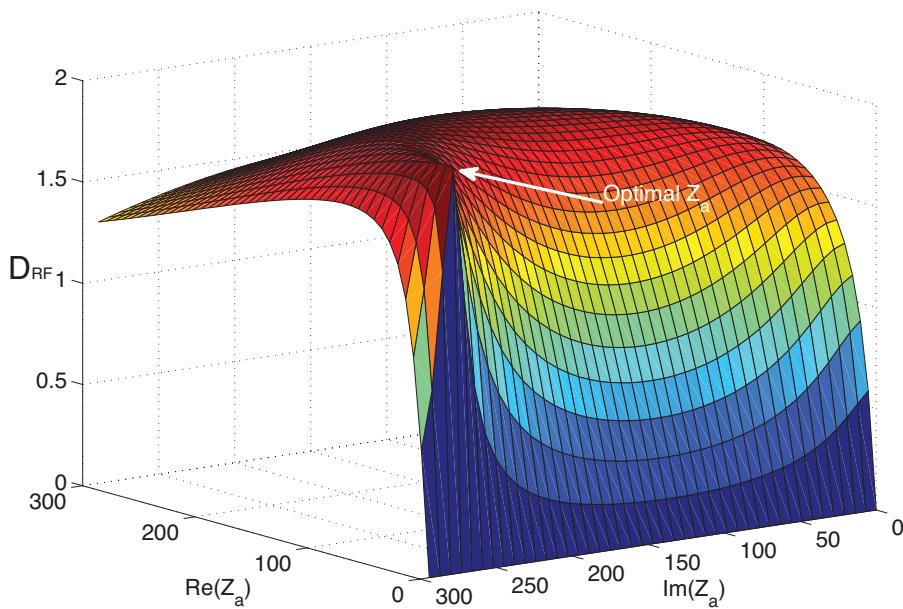
Figure 2.5: 3D plot of real and imaginary value of $Z_a$ vs $D_{RF}$ at 868 MHz. Observe that there exists an antenna with $Z_a = 56.6 + 196.08i$ Ohm that sets $D_{RF} = 1.916$.

that guard-bands are employed between adjacent sensor-bands.

With the utilization of such MAC, the full scale of the proposed network as described in Section 1.3 can be implemented. Particularly, each tag inside a coverage cell that is formed around carrier emitters implements the aforementioned FDMA scheme. Moreover, in order to avoid collisions, the CW emitters are controlled by the reader. Particularly, the latter turns on the emitters in distinct time slots, thus implementing a time division multiple access (TDMA) scheme. Fig. 2.7 depicts the simultaneous operation of 3 tags that employ the FDMA scheme. It is obvious that collision is avoided, while the detection of the frequency shift in subcarrier frequency for a shift in humidity from 20 % to 40 % prominent.

The subcarrier frequency value is controlled by the values of resistors and capacitors in the RC network that is attached to the 555 timer. Therefore, the center frequency as well as the total spectrum that each tag occupies can be controlled by selecting components with appropriate values. Specifically, size of the spectrum band that the $i$-th tag occupies depends on the lowest and
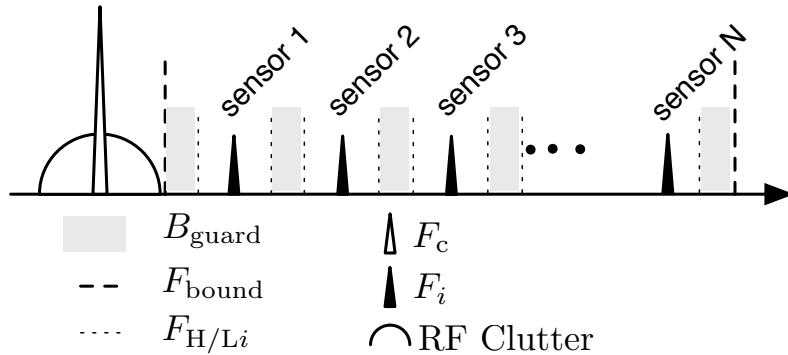
Figure 2.6: Scheme for networking multiple tags. Each tag operates in different frequency bands, while guard bands are set up in between to avoid collision.

highest frequency that is produced by the timer. Let $F_{iL}$ and $F_{iH}$ denote the subcarrier frequency output of th $i$-th tag for lowest and highest frequency, respectively. Then, by using (2.1), the total bandwidth $B_i$ for the $i$-th tag is calculated follows:

$$
\begin{aligned}
B_i &= F_{\mathrm{H}i} - F_{\mathrm{L}i} \\
&\overset{(2.1)(2.3)}{=} \frac{1}{R_i(C_{\mathrm{L}} + C_{\mathrm{p}i})\ln(2)} - \frac{1}{R_i(C_{\mathrm{H}} + C_{\mathrm{p}i})\ln(2)} \\
&= \frac{C_{\mathrm{H}} - C_{\mathrm{L}}}{\ln(2)R_i(C_{\mathrm{L}} + C_{\mathrm{p}i})(C_{\mathrm{H}} + C_{\mathrm{p}i})},
\end{aligned} \tag{2.10}
$$

where $R_i = R_{1i} + 2R_{2i}$ and $C_{\mathrm{L}}$ and $C_{\mathrm{H}}$ are the sensing capacitance values for 0 %RH and 100 %RH, respectively. The values of $R_i$ and $C_{\mathrm{p}i}$ are calculated using (2.1) and (2.10), as follows:

$$
C_{\mathrm{p}i} = \frac{B_i C_{\mathrm{L}} + F_{\mathrm{L}i}(C_{\mathrm{H}} - C_{\mathrm{L}})}{B_i}, \tag{2.11}
$$

$$
R_i = \frac{B_i}{\ln(2)F_{i\mathrm{L}}(C_{\mathrm{H}} - C_{\mathrm{L}})(F_{\mathrm{L}i} + B_i)}. \tag{2.12}
$$

It is obvious that the FDMA scheme is implemented, simply with the utilization of specific capacitor and resistor values, based on the calculations above.
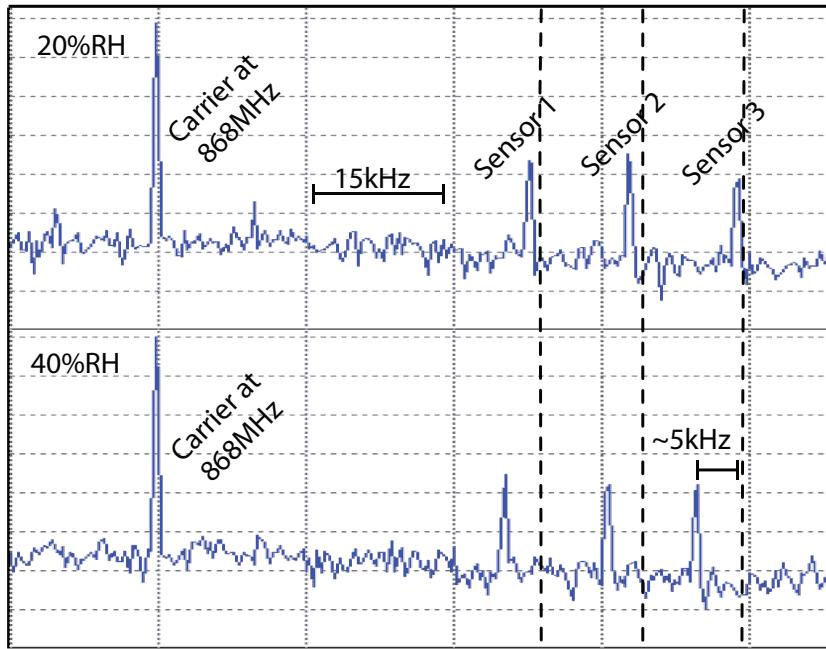
Figure 2.7: Scheme for networking multiple tags. Each tag operates in different frequency bands, while guard bands are set up in between to avoid collision.

## 2.4 Power Supply

The power supply is a crucial component of the tags, since the battery life depends on it. The purpose of the power supply circuitry is to provide a stable voltage to the tag, and to enable the connection of energy harvesting devices. For this purpose, a voltage reference integrated circuit (IC) and two Shottky diodes have been utilized. The diode cathodes are short-circuited (common cathode setup) and connected to the input of the voltage reference IC which is utilized to accommodate battery voltage drops. At each of the diode anodes, a different power source is connected; a 3 V lithium-ion battery (type CR2032) and a small solar panel with an open-circuit voltage of 3.5 V. This simple setup implements a logic 'OR' and allows current to flow from the source with the largest voltage potential to the tag circuitry. As a result the tag is power-supplied by the battery during the night (when the voltage of the solar panel is low) and by the solar panel during the day. Thus, the tag battery lifetime is practically doubled.

The minimum operating voltage of the tag, after measurement is 2.26 V. Moreover, the total power dissipation of the tag depends on multiple factors and is calculated below:

$$P_{\text{tot}} = P_{\text{ch}} + P_{\text{q}} + P_{R_1} + P_{\text{d}}. \tag{2.13}$$

Each of the variables above denote a factor that consumes power. Particularly, $P_{\text{ch}}$ is the average power required for charging the timer capacitors, $P_{\text{q}}$ is the quiescent power dissipated by the timer and the voltage reference IC, $P_{R_1}$ is the power dissipated on resistor $R_1$ and $P_{\text{d}}$ is the power dissipated on the diodes. The components that were utilized in the tag design consume a quiescent power $P_{\text{q}} = 220~\mu\text{W}$. Moreover, the power $P_{\text{d}}$ dissipated at the diodes is calculated as the forward voltage value multiplied by the total current draw of the tag:

$$P_{\text{d}} = \frac{V_{\text{f}}}{V_{\text{cc}}}(P_{\text{ch}} + P_{\text{q}} + P_{R_1}). \tag{2.14}$$

As stated above, due to the astable operation of the timer, the total capacitance $C = C_{\text{p}} + C_{\text{RH}}$ is charged from $V_{\text{cc}}/3$ to $2V_{\text{cc}}/3$ in $(R_1 + R_2)C\ln(2)$ seconds. Therefore, since a first-order $RC$ circuit is formed by $R_1$, $R_2$ and $C$, the voltage $V_{\text{c}}(t)$ which is developed across $C$ and the current $I(t)$, drawn by the power supply, are given by:

$$V_{\text{c}}(t) = V_{\text{cc}}(1 - e^{\frac{-t}{(R_1+R_2)C}}) + V_{\text{c}}(0)~e^{\frac{-t}{(R_1+R_2)C}}, \tag{2.15}$$

$$I(t) = \frac{V_{\text{cc}} - V_{\text{c}}(t)}{R_1 + R_2}, \tag{2.16}$$

where $V_{\text{c}}(0) = V_{\text{cc}}/3$ is the initial condition of the capacitor voltage. Thus, using (2.15) and (2.16), the average power $P_{\text{ch}}$ drawn by the power source,

$V_{cc}$, during a period of $1/F$, is calculated as follows:

$$P_{ch} = F \int_0^{(R_1+R_2)C \ln(2)} V_{cc} \, I(t) \, dt \tag{2.17}$$

$$= \frac{V_{cc}^2}{3(R_1 + 2R_2) \ln(2)}. \tag{2.18}$$

Current flows through $R_1$, while timer output is "low", discharge pin is grounded (and the RF transistor is "on") and thus, the average power drawn by $R_1$ is given by:

$$P_{R_1} = \frac{(1-D)V_{cc}^2}{R_1} \tag{2.19}$$

$$\overset{(2.2)}{=} \frac{V_{cc}^2}{R_1^2/R_2 + 2R_1}. \tag{2.20}$$

During power measurements, it was clear that the power dissipated at $R_1$ during discharge is the largest power consuming factor. For example considering a tag with $R_1 = 5.3$ kΩ, $R_2 = 10.6$ kΩ and $C = 730$ pF operating at $F_{sw} = 74.5$ kHz consumes $P_{ch} = 92$ μW, $P_d = 77$ μW and $P_{R_1} = 385$ μW, resulting in $P_{tot} = 775$ μW. It is obvious that $P_{R_1}$ amounts for approximately half of the power consumed at the tag. A solution would be to increase $R_1$ in order to decrease $P_{R_1}$ as shown by (2.20). However, an increase in $R_1$ would lead in degradation of the communication performance since the implemented receiver depends on the power of the *fundamental* subcarrier frequency of the scatter radio signal. The latter is given by [36]:

$$P(a_1) = \left[ \frac{A\sqrt{2}}{\pi} \sin(\pi D) \right]^2, \tag{2.21}$$

where $D$ is the duty cycle and $A$ is the peak-to-peak amplitude of the pulse signal. For $D = 50$ %, the value of $P(a_1)$ is maximized; when the duty cycle is higher (or lower) than 50 %, the power of the fundamental frequency is decreased. For example, considering the case of two tags with the same subcarrier frequency of 50 kHz, where one tag has $D = 60$ % and the other has $D = 75$ %, then the total power consumption and power of their fundamental

Table 2.1: Example of two tags with different duty cycle $D$.

| $R_1(\text{k}\Omega)$ | $R_2(\text{k}\Omega)$ | $D(\%)$ | $P_{\text{tot}}(\ \mu\text{W})$ | $P(a_1)$ |
|---|---|---|---|---|
| 3.95 | 8.6 | 60 | 989 | $(1.81A^2)/\pi^2$ |
| 10.35 | 5.4 | 75 | 545 | $A^2/\pi^2$ |

frequencies are calculated using (2.1), (2.2) and (2.21). The corresponding results are presented in Table 2.1. It is observed that the sensor/tag with $D = 60$ % consumes approximately 2 times more power than the one with $D = 75$ %, but the latter lacks of power in its fundamental frequency by a factor of 1.81, which in turn will result in less accurate reception, as explained in Section 3.

## 2.5   Calibration

The theoretical relationship of the tag's frequency output value with the %RH value can be calculated using (2.1). However, deviations from non-ideal values of the tag's components (e.g., tolerance of capacitors, resistors, timer etc) result in deviations from (2.1). Moreover, the real-world application of the proposed network targets an *outdoor* field/greenhouse. Such environments exhibit great temperature variations, that significantly affect the operation of the electronic circuits within the tag. As an example, the 7555 timer exhibits a temperature drift of 150 ppm/ºC and, thus, for a tag with nominal subcarrier frequency 50 kHz, a total change of 15º C results to a frequency shift of 112.5 Hz. Hence, for a tag that occupies a bandwidth of 2 kHz, this frequency shift amounts to 5.625 % of the tag's bandwidth and a %RH error of the same order (in percentage).

In order to compensate with both effects and avoid large measurement errors, a calibration process is utilized for each tag [37]. Calibration is one of the most important procedures that affect the accuracy of sensors. It is the process of calculating the transfer function that converts the output of the sensor (in this case subcarrier frequency) to a value of interest (in this case %RH) . The transfer function may utilize more than one variable if the
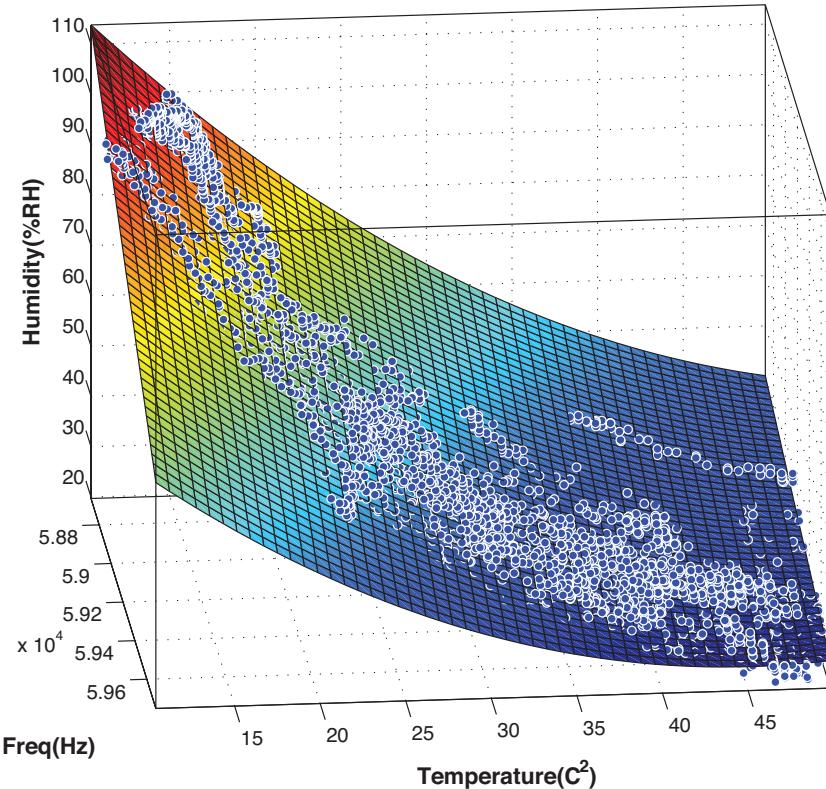
Figure 2.8: Temperature is included as a calibration parameter and thus the characteristic function is the surface RH(F,Temp).

sensor output depends on more than one input stimulus (in this case, both ambient temperature and %RH).

One of the most popular methods for calculating such transfer function is polynomial fitting. The purpose of this method is to find such polynomial function that its outputs exhibit minimal deviation from the recorded outputs for the corresponding stimuli [37,38]. The output of the device under calibration is monitored for multiple stimuli conditions and least squares approximation is applied in order to find the terms of the polynomial. When a single stimuli is monitored (e.g., %RH), the transfer function is two-dimensional and when two stimuli are monitored (e.g., %RH and temperature), the transfer function is three-dimensional (surface).

The tags of this work were calibrated using polynomial surface fitting and utilizing both %RH and temperature as input stimuli [33]. Particularly,
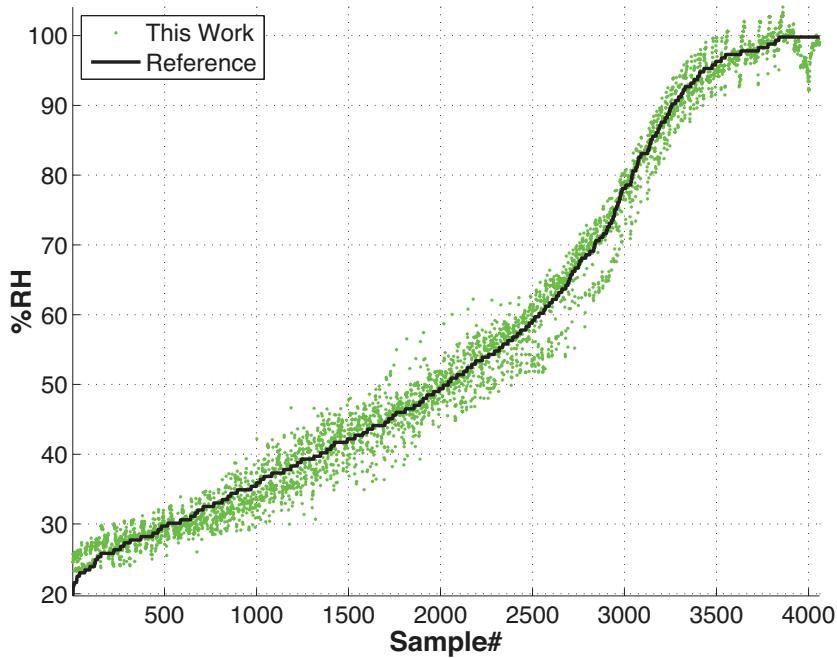
Figure 2.9: Reference vs received %RH measurements.

groups of five sensors were placed outdoors with their capacitive elements in adjacent positions. The Tinytag TGP-4500 from Gemini, which is a high-precision industrial %RH/temperature data-logger, was also placed in close proximity with the tags, for reference. The system was deployed to operate for 3 days and each sensor's subcarrier frequency was monitored at the reader, as analyzed in Section 3, while temperature and humidity from the reference sensor were logged every minute. A total of 4200 samples were collected and time-synchronized, using the timestamps from both the data-logger and the reader. Subsequently, polynomial surface fitting was applied in order to produce the three-dimensional transfer function, which is shown in Fig. 2.8. The calibration process should be applied for each sensor before the incorporation in the network. That is due to the tolerance of the capacitance/resistance as well as the timer, that affects the switching frequency of the tag.

In order to characterize the measurement accuracy, the collected temperature and subcarrier frequency data were utilized as inputs for the transfer function. The output of the transfer function was then compared to the
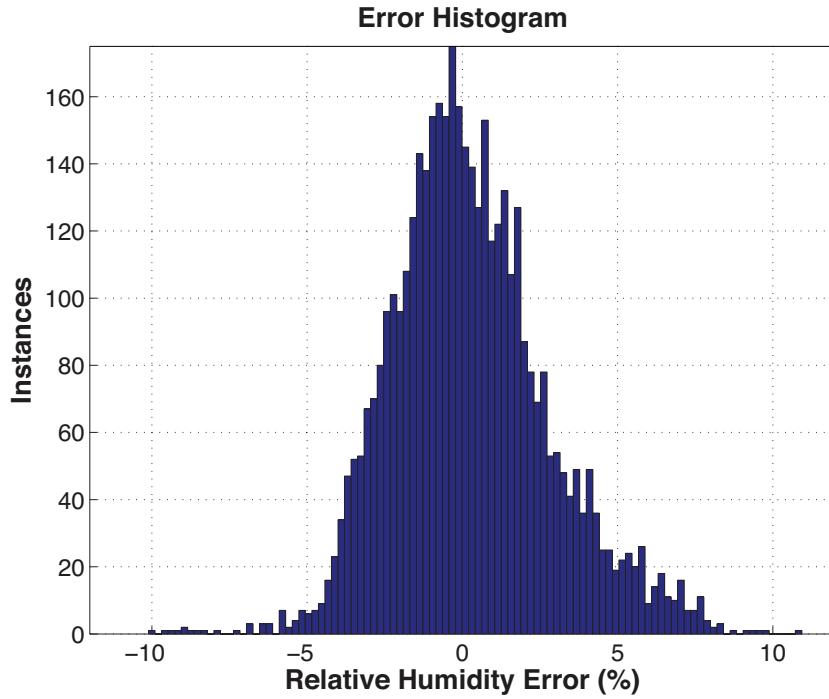
Figure 2.10: Measured %RH error histogram.

reference results from the data logger. The resulting relative humidity measurement error histogram and measured values are depicted in Figs. 2.9 and 2.10, respectively, operating a reference sensor and the calibrated tag in the 10-50 °C temperature range. The root mean squared error (RMSE) and the mean absolute error of the particular calibrated tag were 2.5 %RH and 1.9 %RH, respectively. Also, for 95 % of the samples, where humidity varied from 20 %RH to 100 %RH, the absolute error was less than 5 %RH. For the case of tag calibration under constant temperature of 25 °C, the corresponding accuracy was higher, exhibiting an RMSE of 0.86 %RH and a mean absolute error of 0.63 %RH. Similarly, for 95 % of the samples at 25 °C, the absolute error was less than 1.8 %RH [33].

# Chapter 3

# Scatter Radio Network Reader

## 3.1 CFO Compensation and Subcarrier Estimation

I Q

N Samples Buffer → CFO Comp. → FFT → BPF

M times ACC ← MAX

Histogr. Filt.

Sav.Gol. Filt.

%RH(F,T)

%RH
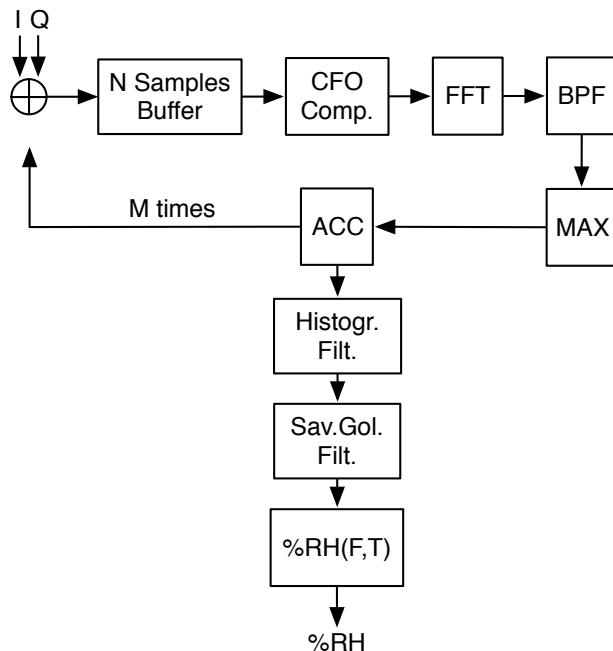
Figure 3.1: Sensor's subcarrier frequency value is estimated using periodogram detection. After a set of data is collected, the aforementioned filtering is applied.

One of the most important components of the scatter radio WSN developed was the receiver [33]. The receiver is responsible for the estimation of the frequency of the incoming scattered subcarrier signals, the de-noising as well as the extraction of the %RH data by utilizing the corresponding transfer function of each tag. In order to facilitate the development process while

keeping the cost low, the Ettus USRP N200 software-defined homodyne radio platform was utilized and connected to a simple laptop that acted as the host. The USRP down-converts the signals to the baseband using a homodyne architecture and transfers the in-phase (I) and quadrature (Q) digitized signal samples to the host via gigabit Ethernet. Subsequently, the samples are saved to a queue and processed in software that is implemented in MATLAB. A diagram of the receiver that was implemented is illustrated in Fig. 3.1 and a detailed analysis of its functionality is provided below.

The first process that is executed on the receiver is the so called carrier frequency offset (CFO) estimation-compensation. The purpose of this process is to minimize the effect of the difference in frequency between the carrier emitter, and the USRP that down-converts the signals from UHF at 868 MHz to baseband. This effect results in a deviation between the real and the estimated values of the subcarrier signals by an amount on the order of 1-2 kHz and is mainly dependent on the temperature of the USRP (therefore it changes over time and needs to be constantly monitored). The CFO *estimation* is implemented by calculating the difference between the nominal carrier value and the estimated one. The periodogram of the received signals is calculated; the nominal carrier value is located at frequency 0, while, the real carrier frequency value is estimated by locating the frequency component with the highest amplitude. Subsequently, CFO *compensation* is implemented by frequency-shifting the received samples according to the calculation of the difference between the real and nominal carrier frequency values.

For the estimation of each subcarrier frequency, the periodogram of the (frequency-shifted) samples is calculated once more. Followingly, for each tag, a filter is applied such that the frequency components that reside outside the corresponding tag's *fundamental* frequency band (which is a-priori known to the receiver), are set to zero. Finally, the subcarrier frequency value is estimated by locating the frequency with the maximum power, among the remaining frequency components. In other words, the fundamental subcarrier

frequency of the $i$-th tag is calculated based on the equation below:

$$\hat{F}_i = \arg\max_{F \in [F_{\mathrm{L}i}, F_{\mathrm{H}i}]} |X(F)|^2, \tag{3.1}$$

where $X(F)$ is the Fourier transform of the received signal and $F_{\mathrm{L}i}$, $F_{\mathrm{H}i}$ mark the a-priori known lowest and highest possible frequency output of the $i$-th tag.

## 3.2 Filtering

The error that is introduced from the thermal noise at the receiver, degrades the communication performance. For this reason, a two-phase filtering process that compensates the errors was implemented. The filtering process takes advantage of the fact that relative humidity changes with a slow rate, and therefore samples within a short period of time exhibit small deviation from one another.

Initially all the $\hat{F}_i$s are estimated (as denoted in (3.1)) over a period of 10 minutes and stored in an accumulator in the form of the vector $\vec{\hat{F}}_i$. Subsequently, the first phase of the filtering process takes place; a histogram over the $\vec{\hat{F}}_i$ with 200 bins is calculated that corresponds to a frequency resolution of 10 Hz for a sensor's bandwidth of 2 kHz. Over the 10-minute period that the samples are collected, %RH and as a result, the subcarrier frequency of each tag, does not exhibit a large variation. Hence, the most frequent values in the histogram, denote the true value of the subcarrier frequency, while the noisy outliers are less frequent. An example of such histogram is depicted in Fig. 3.2 in which, one can observe that the most frequent $F_i$s are located in a distinct frequency region.

Subsequently, this region is located by utilizing a sliding window of length $N_B$ bins across the histogram and calculating the in-window sample cardinality. The most frequent $F_i$s, as estimated by the sliding window are kept intact and their mean value $\mu$ is calculated. The rest of the $F_i$ values that do not belong to the region that was found previously, are set to $F_i = \mu$. Histogram filtering techniques are mostly utilized in image processing for de-
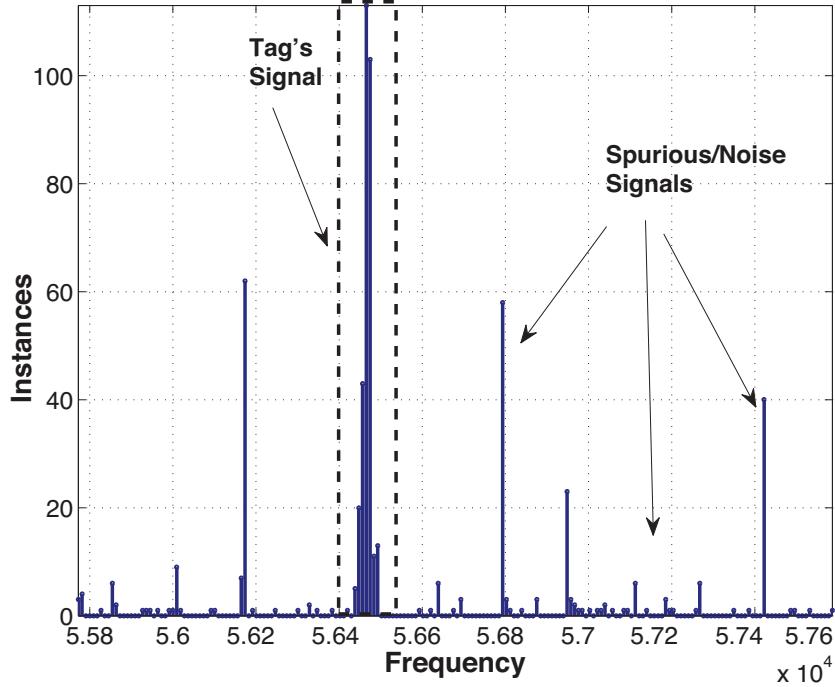
Figure 3.2: Histogram filtering: A set of measurements is collected and their histogram is calculated. Only measurements within a certain range and with the highest occurrence are kept.

noising and smoothing and an example is demonstrated in [39]. The effect of the histogram filtering is depicted in Fig. 3.3; noise reduction is prominent.

However, it is obvious from Fig. 3.3 that data smoothing is required. This is were the second phase of the filtering process takes place, with the utilization of a Savitzky-Golay filter [40]. Savitzky-Golay filtering is largely adopted in data smoothing applications, as in [41] and has its roots back in 1964 [42]. Data smoothing of the measurement data set is implemented via the utilization of local least-squares polynomial approximation. Work in [40] provides an extensive report on the low-pass characteristics of such filter, and discusses the effect on the cutoff frequency and the response of the filter versus specifications, such as the polynomial rank and the cardinality of the subset that is subject to interpolation. Through experimentation with real data, it was found an appropriate polynomial order and subset size are 3 and 201, respectively.
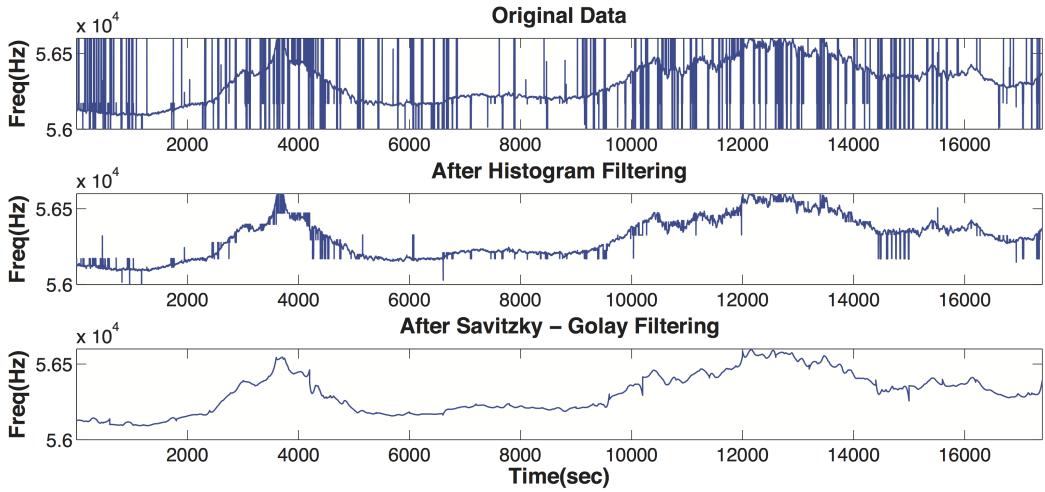
Figure 3.3: Filtering process of received measurements. Histogram filtering followed by Savitzky-Golay filtering is applied.

An example of the filtering process is illustrated in Fig. 3.3. In is noted that with the utilization of the above process, the measurement error is significantly reduced. Specifically, in some cases, the resulting mean error is reduced even by one order of magnitude as noted in the next section where extensive experimental results are offered.

## 3.3 Point to Point Setup and Experimentation

For the communication performance characterization of the proposed WSN in terms of measured error and maximum communication range, extensive real-world experiments were conducted. Particularly, a complete point to point link, set up in bistatic topology was utilized. The setup was composed of a receiver-reader implemented on the USRP N200 platform, a carrier emitter of the CW and a tag with center subcarrier frequency at 75 kHz and a bandwidth of 2 kHz. The carrier emitter is a Silabs Si1004 development kit that was programmed to produce a CW at 868 MHz with a transmission power of 20 mW. It is important to note that the maximum permissible limit which is imposed by European directives is 3.2 W (EIRP). All the
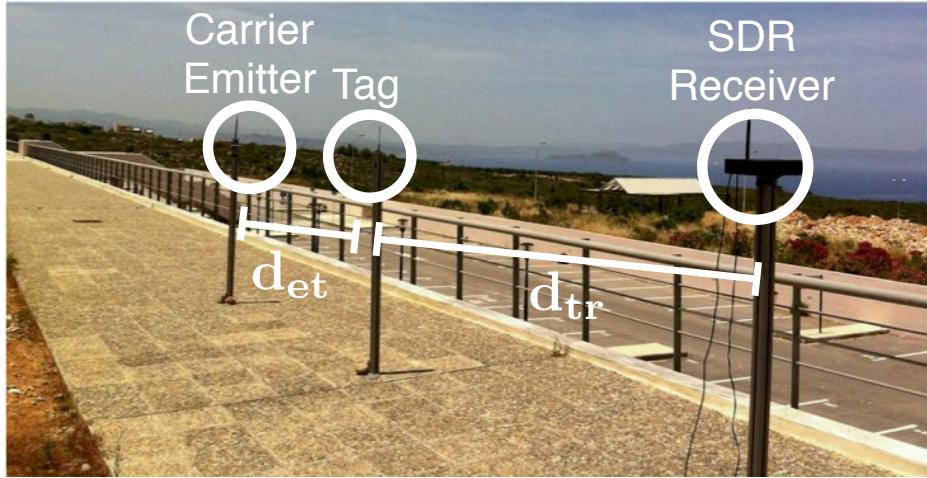
Figure 3.4: Bistatic setup in outdoor deployment for characterizing the communication range of a point to point link. Each device is set up in poles of 1.5 m height.

aforementioned devices were properly installed on poles of 1.7 m height and the system is depicted in Fig. 3.4.

The purpose of the testbed was to investigate *only* the communication performance. Therefore, it was desired to exclude the calibration error which is thoroughly analyzed in Section 2.5. Hence, instead of comparing the estimated with the reference %RH values (as in Section 2.5), the estimated subcarrier frequency at the reader was compared to the output frequency on the corresponding tag. The output frequency of the tag was monitored using a frequency data-logger and timestamps were utilized to synchronize the samples.

Numerous experiments where conducted, and the effect of the emitter-to-tag distance ($d_{et}$), the tag-to-reader distance ($d_{tr}$), the receiving window duration per measurement ($T_w$) and the two-phase filtering was examined. The root mean squared error (RMSE) and mean relative error (MRE) were the metrics that were utilized for evaluation of the accuracy performance of the proposed WSN. The MRE is defined as the quotient of the mean absolute error in Hz with the tag's bandwidth, multiplied by 100, which provides an estimation of the corresponding %RH error. All results are depicted in Table 3.1, where each row corresponds to a different experiment.

Table 3.1: Communication Distances and Accuracy

| # | $d_{et}$(m) | $d_{tr}$(m) | $T_w$ (ms) | RMSE(Hz) pre-filt. | RMSE(Hz) post-filt. | MRE(%) pre-filt. | MRE(%) post-filt. |
|---|---|---|---|---|---|---|---|
| 1 | 2 | 134 | 1000 | 7.38 | 3.12 | 0.14 | 0.12 |
| 2 | 2 | 134 | 100 | 4.14 | 3.94 | 0.11 | 0.15 |
| 3 | 2 | 134 | 10 | 12.34 | 8.52 | 0.51 | 0.28 |
| 4 | 8 | 128 | 1000 | 8.73 | 7.07 | 0.16 | 0.22 |
| 5 | 8 | 128 | 100 | 3.20 | 11.63 | 0.10 | 0.34 |
| **6** | **8** | **128** | **10** | **440.34** | **26.78** | **12.04** | **1.05** |
| 7 | 16 | 120 | 1000 | 9.42 | 4.78 | 0.16 | 0.19 |
| 8 | 16 | 120 | 100 | 27.05 | 4.05 | 0.19 | 0.17 |
| 9 | 16 | 120 | 50 | 202.62 | 30.19 | 2.52 | 1.33 |
| **10** | **16** | **120** | **25** | **414.28** | **35.69** | **9.85** | **1.54** |
| 11 | 24 | 112 | 1000 | 73.50 | 7.53 | 0.53 | 0.31 |
| 12 | 24 | 112 | 100 | 337.45 | 48.38 | 6.72 | 2.02 |
| **13** | **24** | **112** | **50** | **499.77** | **78.43** | **14.72** | **3.54** |
| 14 | 32 | 104 | 1000 | 530.37 | 126.65 | 12.36 | 5.02 |
| 15 | 32 | 104 | 100 | 661.34 | 251.82 | 22.01 | 12.45 |
| 16 | 52 | 84 | 1000 | 44.68 | 5.00 | 0.22 | 0.20 |
| 17 | 52 | 84 | 100 | 68.94 | 5.54 | 0.34 | 0.22 |
| **18** | **86** | **50** | **1000** | **59.25** | **8.07** | **8.13** | **3.14** |
| 19 | 86 | 50 | 100 | 80.79 | 6.86 | 0.55 | 0.30 |
| 20 | 96 | 40 | 1000 | 3.21 | 4.16 | 0.1 | 0.19 |
| 21 | 96 | 40 | 100 | 4.55 | 3.67 | 0.08 | 0.15 |
| 22 | 96 | 40 | 25 | 421.60 | 49.85 | 7.37 | 2.25 |

It is obvious that there is a significant improvement with the utilization of the filtering process. Particularly, the highlighted experiments 6, 10, 13, 18, demonstrated an important MRE reduction which in most cases approaches one order of magnitude. One of the distinguished cases is the experiment 13, where the MRE of 14.72 % was reduced to 3.54 %. This experiment indicated that in the particular topology, without the utilized filtering, the sensor would be unusable even for the target environmental monitoring application. Therefore, it is evident that with the proposed filtering process, the signal-to-noise ratio (SNR) is effectively improved, which allows for longer communication distances.

However, the filter that was implemented is not optimal in all SNR cases. Particularly, in the high-SNR experiments 5 and 20, the utilization of filtering apparently increased MRE. This is due to the fact that in the particular ex-

periments, most frequency estimations were correct due to the high SNR and therefore, a small amount of them was treated as erroneous. Nevertheless, error increase is on the order of 0.1 % which is too small to be important.

Finally, it is noted that the end-to-end accuracy depends on two types of errors: the reception error, which is relative to the noise and sensitivity of the receiver, and the sensing error, which is due to the capacitive %RH sensor and the capacitance-to-frequency converter. The sensing error is extensively presented in Section 2.5 and illustrated through Figs. 2.9 and 2.10, while the reception error is described through Table 3.1. The end-to-end accuracy can be calculated by exploiting the independence of the two errors with the following equation [33]:

$$\text{RMSE} = \sqrt{\text{RMSE}_s^2 + \text{RMSE}_r^2}, \tag{3.2}$$

where $\text{RMSE}_s$, $\text{RMSE}_r$ is the RMS value of the sensing and the reception error in %RH units, respectively. In order to convert the RMSE value as presented in Table 3.1 from Hz to %RH units, the corresponding RMSE value must be divided by the tag's bandwidth (in all cases 2 kHz) and be multiplied by 100. For example, in the case 13 of Table 3.1 the resulting RMSE is 78.43 Hz. That corresponds to an $\text{RMSE}_r = 100 \cdot 78.43/2000 = 3.92$ %RH error. Moreover the sensing error due to the conversion of capacitance to frequency exhibits an $\text{RMSE}_s = 2.5$ %RH (as shown in Section 2.5). Therefore, by utilizing (3.2), the end-to-end RMSE for that particular case equals to 4.65 %RH.

## 3.4 Comparison with Classic WSNs

It is obvious that the node cost of the proposed WSN, compared to classic WSNs is significantly lower due to the fact that the RF front-end is composed of a single transistor-switch. This section provides a power consumption comparison between a classic WSN node for the transmission of a single data packet and the tag of this work.

The method for decreasing the energy consumption per measurement in classic radio WSN nodes is the so called duty cycling and it regards periodical

transmission and falling into idle mode of the node. With the exploitation of duty cycling the battery lifetime is highly extended. Regarding this work, duty cycling would further decrease the required energy requirements per measurements, since the tags of this work already consume low power.

The experiments of the previous section provided an indication about the time that the sensors should remain 'active' and scatter the %RH measurement with an acceptable error. However, a communication tradeoff is prominent since a decrease in the duration of the receiving time window $T_{\mathrm{w}}$ results in decreased number of received signal samples at the receiver. In turn, this results in degraded SNR and communication performance. Table 3.1 demonstrates the fact that $T_{\mathrm{w}}$ can be reduced down to 10 ms for relatively small $d_{\mathrm{et}}$ distances as in experiment 3. On the other hand, for longer communication distances, as in experiments 8, 12, 17, 19, 21, the minimum required $T_{\mathrm{w}}$ for reliable communication is 100 ms. Additionally, for all cases, each setup with a $T_{\mathrm{w}}$ of 1 sec exhibits better communication performance compared to narrower sampling windows.

A classic WSN node typically consists of an active, low-power ZigBee-type radio and a microcontroller unit. The energy consumption of such a node is calculated by:

$$E_{\mathrm{wsn}} = \frac{N_{\mathrm{b}}}{F_{\mathrm{tx}}} P_{\mathrm{tx}}, \tag{3.3}$$

where $N_b$ is the number of bits per measurement transmission, $F_{\mathrm{tx}}$ is the data rate (in bits per second) and $P_{\mathrm{tx}}$ is the power consumption (in Watts). On the other hand, the energy per measurement for the developed analog humidity sensor with scatter-radio is given by:

$$E_{\mathrm{bs}} = T_{\mathrm{bs}} \ P_{\mathrm{bs}}, \tag{3.4}$$

where $T_{\mathrm{bs}}$ denotes the receiving window duration (in sec) needed for reliable scattering of humidity measurement and $P_{\mathrm{bs}}$ is the power consumption of the sensor (in Watts). The two approaches (i.e. the active radio module and the scatter radio tag) were compared for energy consumption (in Joules per

Table 3.2: Comparison of energy consumption per measurement in the proposed and classic WSN radio modules.

| Comm. Module | Bit-rate (kbps) | Power (mW) | Time "on" (ms) | Energy (mJ/measurement) |
|---|---|---|---|---|
| TI CC2500 | 2.4 | 42.4 | 26.7 | 1.132 |
| TI CC2500 | 10 | 42.4 | 6.4 | 0.271 |
| TI CC2500 | 100 | 42.4 | 0.64 | 0.03 |
| TI CC2500 | 250 | 42.4 | 0.256 | 0.01 |
| This Work | – | 0.72 | 1000 | 0.72 |
| This Work | – | 0.72 | 100 | 0.072 |
| This Work | – | 0.72 | 50 | 0.036 |
| This Work | – | 0.72 | 10 | 0.007 |

measurement) and the results are provided in Table 3.2. A typical scenario was exploited for the active WSN node which is the transmission at 0 dBm of a 64 bits packet, with the utilization of the popular Texas Instruments CC2500 radio module [43]. As one can observe, the tag outperforms the CC2500 for data rates smaller than 100 kbps. Additionally, for all bit-rate cases the tag consumes smaller energy than the active radio module when a receiving window of 10 ms is utilized.

It is obvious that accuracy is compromised with the use of a smaller $T_w$. Nevertheless, for the target applications of the proposed WSN (e.g., %RH monitoring inside a greenhouse), accuracy can be relatively low, and an MRE of 5 %RH is tolerable. As a result, regardless of the decrease in accuracy of measurement, smaller sampling windows could be utilized in specific applications. For example, the sampling window of 10 ms exhibits an MRE of 1.05 %RH; accuracy which is totally tolerable for the target applications.

The results that were discussed in this section, show that the proposed WSN is able to communicate reliably with ranges on the order of 100 m. Most importantly, low cost and low power consumption specifications were met in order to facilitate the development of large scale networks.

# Chapter 4

# Testbeds

## 4.1 Relative Humidity Monitoring Inside a Tomato Greenhouse
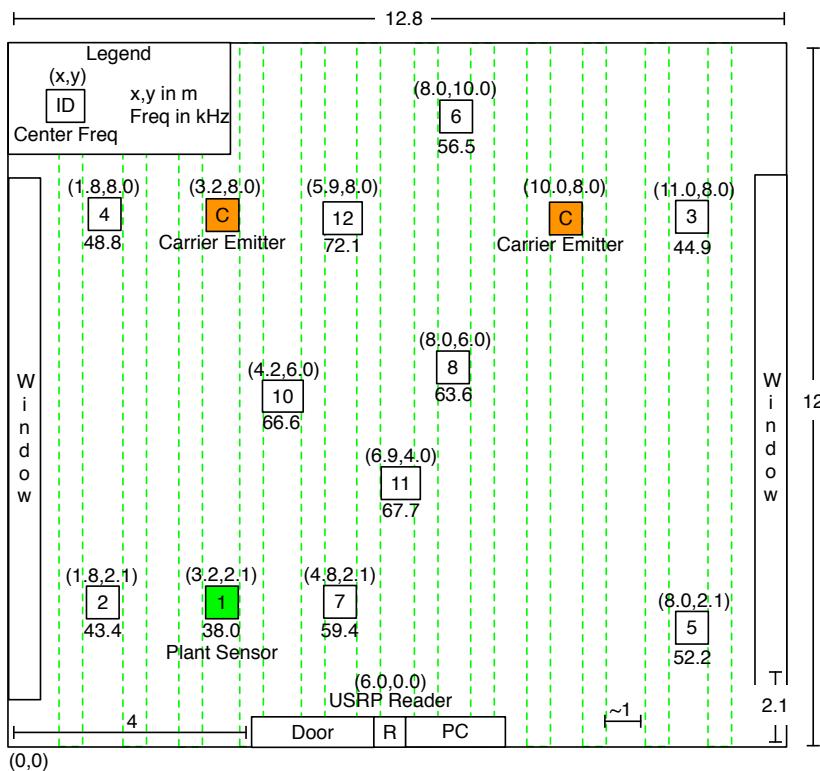


Figure 4.1: Experimental network topology. 10 %RH sensors, 1 plant voltage sensor and 2 carrier emitters with transmit power at 20 mW were deployed.

Monitoring environmental humidity is a highly desired procedure in greenhouse facilities because %RH is a variable that affects crops significantly. For example, high %RH values promote the development of diseases such as *Botrytis cinerea* [23]. Apart from that, conditions with saturated environ-

Figure 4.2: Photo of the deployment inside the greenhouse.

mental humidity affects the plants' evaporation mechanisms thus decreasing their ability to absorb important nutrients [24]. The WSN that was developed is a highly suitable candidate for %RH monitoring inside a greenhouse. Therefore, for the evaluation of this work's performance in a real-world scenario, a WSN was set up and deployed in a greenhouse for tomato cultivation at the Mediterranean Agronomic Institute of Chania (MAICh, `www.maich.gr`) [33].

Particularly, the network was composed of 10 tags identical to the ones described in Chapter 2 among with two carrier emitters . The carrier emitters were utilized so as to increase the coverage of the network. Moreover, in order to avoid collisions, the CW was emitted from each device alternatively at 20 mW power. Fig. 4.1 depicts the topology of the network, where the locations of all devices that where installed (tags, emitters receiver, PC) are highlighted. Moreover, in order to achieve insulation from humidity and dust and place the antennas in high positions, each tag was installed in IP65-rated enclosures and hanged from the ceiling. Fig. 4.2 illustrates the setup after installation of all components.

In order to implement the multiple access scheme that was described in Section 2.3, each tag was employed with resistors and capacitors, with values that were calculated according to (2.11) and (2.12). One can observe from Fig. 4.3 that collision is obviously avoided and that each tag operates at a distinct frequency band. Moreover the receiver that was described Section 3.1
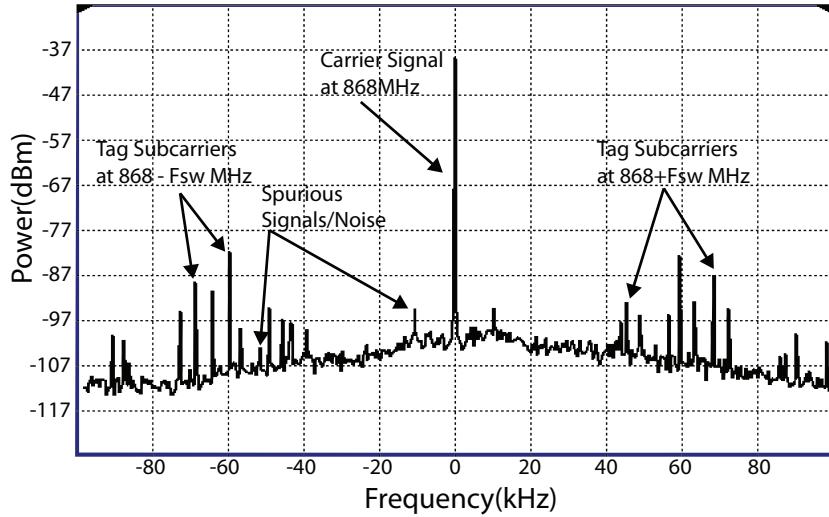
Figure 4.3: Periodogram from multiple sensors in the greenhouse. Each tag operates in a distinct frequency band.

was employed, utilizing the Ettus USRP N200 SDR.

For the processing of the received scatter radio signals, a modest capabilities laptop was utilized, that also acted as host for the USRP. The laptop and the USRP were placed in insulating enclosures and were powered through an uninterruptible power supply (UPS) unit. Finally, remote control software was installed in order to facilitate experimentation, while the collected data where uploaded to a remote database in order to be viewed and downloaded from the corresponding web interface.

A sample data collection from approximately 48 hours of monitoring is illustrated in Fig. 4.4. It is evident that all sensor exhibit similar behavior with slight variations. This is due to the fact that the microclimatic environmental conditions surrounding each tag are not common. One of the distinguishable examples is that the sensors that are placed in close proximity to the windows measure on average lower %RH values. This effect is highly observable during the night, where humidity tends to saturate at a particular value.
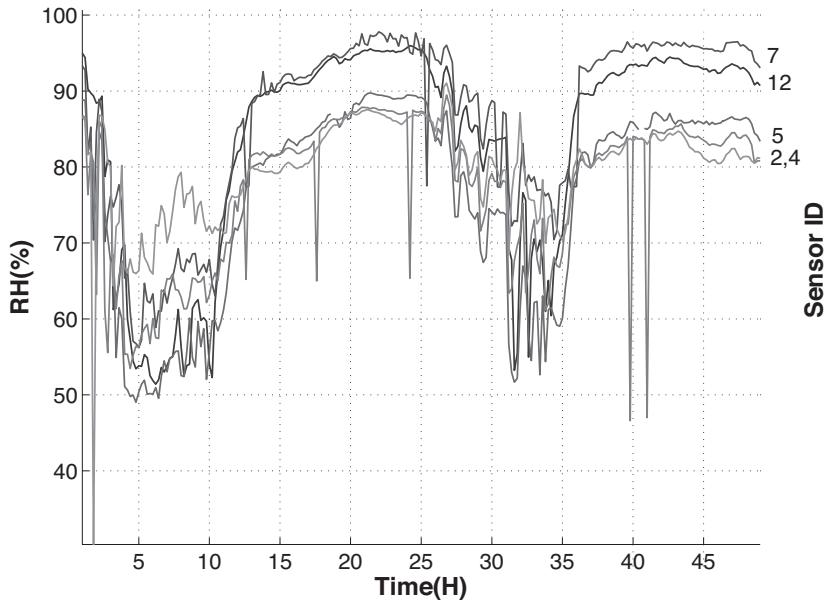
Figure 4.4: Data collected from multiple tags inside the tomato greenhouse for a total of 48 hours. Differences in %RH are due to the variability of microclimatic conditions across the greenhouse (e.g., tags closer to the window exhibit smaller %RH values).

## 4.2 Over The Air Programmed Testbed for Digital Tags

### 4.2.1 Overview

In parallel with the work that was described throughout this thesis text so far, another project was developed and the results published in [44]. The project regards the development of a testbed for scatter radio network research, with the utilization of the digital tags that were designed in [45]. This section describes the design and development of this testbed.

Particularly, testbeds for classic WSNs have been extensively researched and one of the typical examples was demonstrated in [46]. The typical architecture of such testbeds consists of interface boards that monitor the devices under test (in this case WSN nodes) and a gateway that collects the data from the interface boards via a high level network interface (e.g., Ethernet, 802.11)
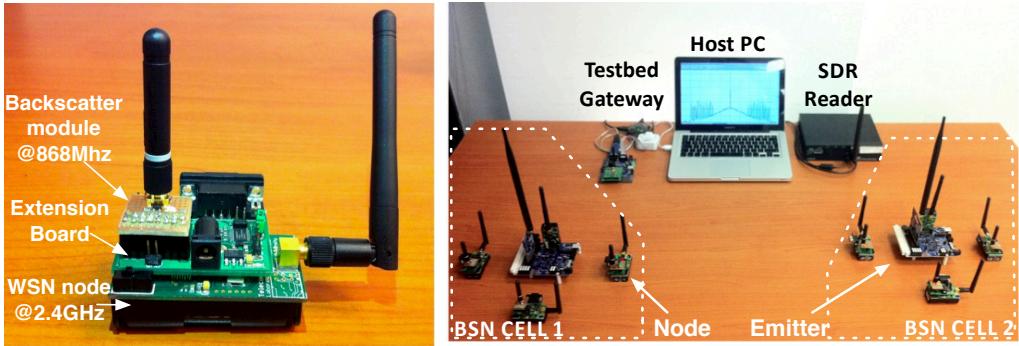
Figure 4.5: Left: Hybrid testbed node. Right: Experimentation testbed.

On the other hand, similar tools for scatter radio network research are limited. One of the few examples was demonstrated in [47], where a testbed was developed for measuring the performance of RFID antennas. However, this setup is limited only in the characterization of antenna microwave parameters. This chapter describes the hardware and software components for the development of a testbed for scatter radio WSN research.

The complete testbed setup is depicted in Fig. 4.5-right and its architecture is illustrated in Fig. 4.6. The devices under test (DUT) consist of the Silabs C8051F320 MCU (instead of a 555 timer) that controls the switching frequency of the transistor.The MCU also controls a TI CC2500 radio which is utilized for the high level control link at 2.4 GHz. The hybrid node that was fabricated is depicted in Fig. 4.5-left. The node operates both as a semi passive scatter radio tag and as a monitoring device that incorporates control and debugging functionality. Additionally, the tag software and the monitoring software are implemented in software in order to be completely independent to one another. Moreover, the emitters of the CW, which are implemented on Si1004 DKs, are remotely controlled and, finally, the reader is implemented on the Ettus USRP software defined radio (SDR) platform.

The host PC that controls the USRP also hosts the testbed gateway which is implemented with C8051F320 development kit and a TI CC2500 radio module. The latter is responsible for transmitting executable code and control packets to the carrier emitters and the tag/nodes over a reliable 2.4 GHz link. Moreover, the gateway exchanges debugging messages and
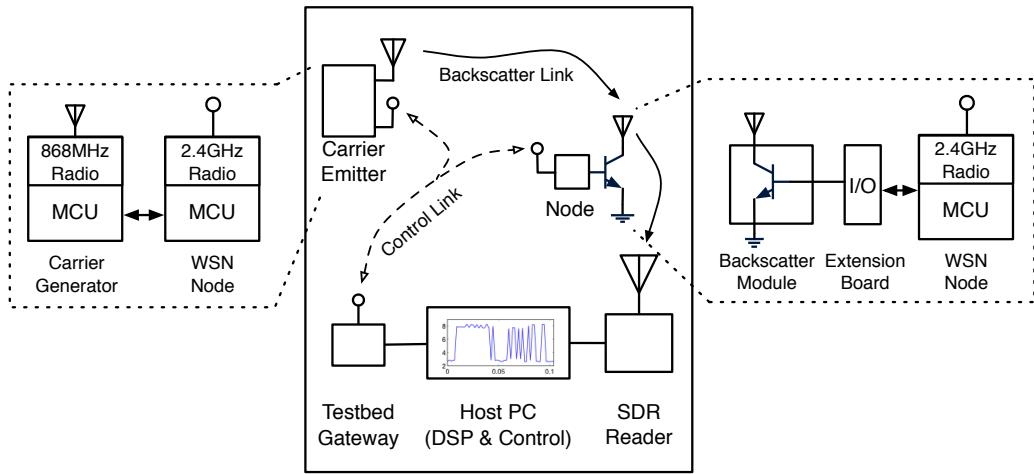
Figure 4.6: Center: Testbed overview. Left: Carrier emitter. Right: hybrid node architectures.

feedback from the DUTs.

Various scatter radio communication topics were researched with the utilization of the testbed, such as detection schemes, resource allocation techniques, networking algorithms, as well as RF hardware (e.g switching transistors) and antennas.

## 4.2.2 Benefits

Through the utilization of the scatter radio testbed the engineer is benefited from mobility–portability, over the air programmability (OTAP), debugging and network monitoring, high level of software and hardware flexibility, with low cost and reduced experimentation time.

Portable operation of a network testbed is a critical feature, especially for outdoor experimentation. In order to evaluate environmental sensing capabilities of the network, the testbed was deployed outdoors in a topology that is depicted in Fig. 4.7. Particularly, six tag-nodes were placed around the emitter of the CW up to a distance of 17 m away from the reader. One can also observe the USRP connected to a host PC, among with a portable spectrum analyzer that is utilized for debugging purposes. The USRP requires power supply but can be modified in order to be completely
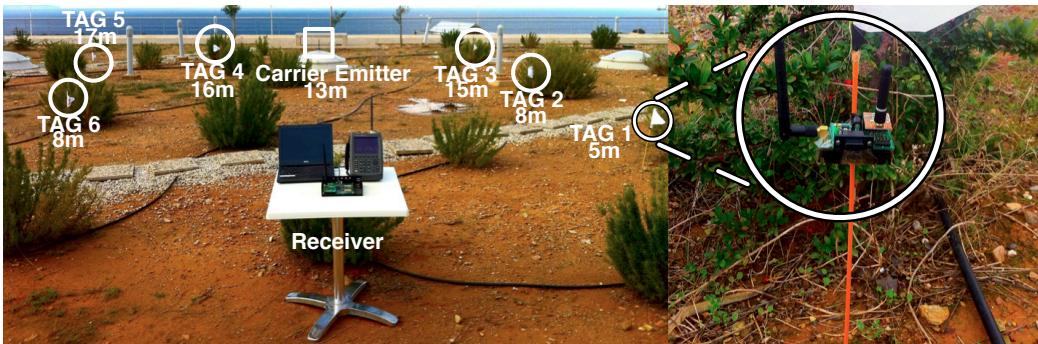
Figure 4.7: Remotely programmable testbed and hybrid node, outdoor deployment.

portable using the work done in [48].

Moreover, over the air programming (OTAP) is an important feature that was implemented for the purposes of this work. With the utilization of OTAP, the tag-nodes can be wirelessly programmed, thus accelerating the overall software development process. For example, the network of Fig. 4.7 requires a total programming time of approximately 12 minutes, whereas with OTAP this time is reduced to 12 seconds, which is two orders of magnitude less.

The components that were used for the fabrication of the testbed exclusively consist of low-cost, commodity and in-house fabricated hardware and are easily interchangeable. This includes the scatter radio hardware like the RF switch, the antenna and various sensors which can easily be installed through general purpose input (GPIO) pins. Software configuration is implemented in C programming language. Using C, one can control the frequency and power of the CW that the corresponding emitters produce and, also, program applications to the tag-nodes. Finally, the total cost of the testbed is approximately 1320 € with the PC and the USRP costing 1140 €.

## 4.2.3 Hardware and Software

The hybrid node was developed with the classic WSN testbed architecture in mind. Particularly, the node acts both the monitor and the DUT. This is implemented with the connection of a module that accommodates a scatter
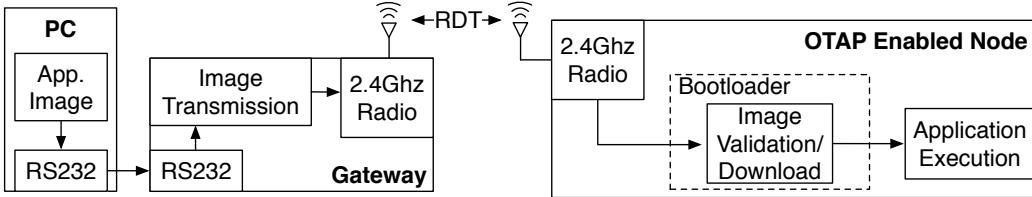
Figure 4.8: Over the air programming block diagram.

radio front-end like the one described in Section 2.2, to the expansion board of the WSN node that was developed in [49]. The 2.4 GHz link is utilized as the control and programming link, while scatter radio communication is implemented at 868 MHz through the scatter radio module. Fig. 4.5-left depicts the implemented node and Fig. 4.6 (right) depicts node architecture. Additionally each of the carrier emitters is connected to a WSN node and is controlled via the 2.4GHz thus allowing for full control of the network. Finally, as it was described in previous sections, the USRP SDR, provides the necessary flexibility for in-depth communication experimentation ranging from physical to application layer.

Regarding the software, one of the most important components of the testbed, is the software that implements OTAP. One can observe the OTAP software architecture in Fig. 4.8 , where the bootloader, the gateway firmware and the application software components are depicted. The procedure of programming the network follows. Initially, the user writes in C and compiles the application that will be downloaded to the tag-nodes. The executable program is transferred to the gateway from the host PC via RS232 interface. The gateway firmware is responsible for compressing the executable and transferring it reliably to the tag-nodes via the 2.4 GHz link. Subsequently, the bootloader firmware that is installed on each node, is responsible for receiving the executable image file, validate it and initiate the application execution. With the utilization of this procedure, each node can be programmed in approximately 2 seconds which is 2 orders of magnitude less than the classic programming approach. Moreover, physical contact through hardware programmers that could damage the tag-nodes in the long term is avoided.
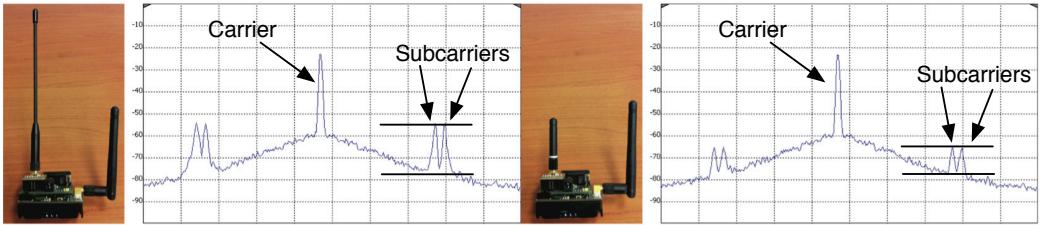
Figure 4.9: Received power spectrum of a half-wavelength and a quarter-wavelength antenna with fixed tag-reader distance. The switching (i.e sub-carrier) frequencies are clearly visible. The quarter-wavelength antenna scattered signal has fairly smaller amplitude than the one scattered from the half-wavelength antenna.

It is important to note that important functionalities where carefully implemented on each component. This includes, the compressing of the image file from the gateway, the reliable data transmission (RDT) protocol, the checksum image file validation from the bootloader, along with every functionality that was implemented in order to avoid undesired errors through the programming process (e.g., watchdog timing on bootloader). All the details of the implementation are included in [50].

## 4.2.4 Applications

A short description follows, of the implemented scenarios and applications that were examined with the utilization of the testbed.

**RF/Microwave Research for Scatter Radio:** One of the necessary procedures for scatter radio research is the experimentation with various designs and components especially on the RF front-end part. With the utilization of the testbed, it is straightforward to install commodity or prototype antennas as well as different RF switches, without re-designing the whole tag-node. This allows rapid testing of scatter radio link budgets and RF front-end performance. For example, Fig. 4.9 illustrates the variation in the received power spectrum for a quarter-wavelength and a half-wavelength antenna (tag-node in fixed location).
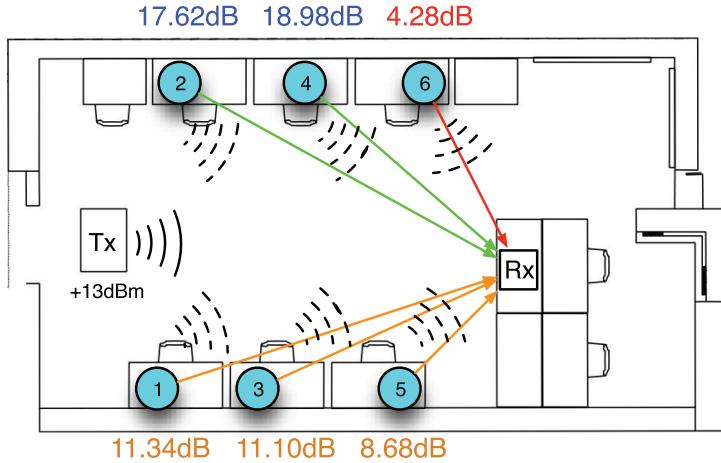
Figure 4.10: Measured SNR values per scatter radio tag in lab deployment.

**Physical Layer Communication:** Additionally, it is feasible to examine the performance of various receiver designs, as well as communication schemes, along with various tradeoffs. Particularly, on-off-keying (OOK) and frequency-shift-keying (FSK) modulations, along with the corresponding receivers were implemented and their performance was evaluated in an indoor deployment shown in Fig. 4.10. Experimentation was facilitated due to the fact that the effect of channel fading was avoided with the utilization of OTAP. Noise and received carrier power (emitted at +13 dBm) were estimated at the reader, followed by a per-tag SNR estimation of the subcarrier signals.

Additionally, scatter radio communication comes with various idiosyncrasies such as the CFO (discussed in Section 3.1) and the RF clutter. The latter is introduced due to emitter's inherent phase jitter and the nonlinearities of its power amplifiers, and results in increased noise floor around the frequency of the CW. The effect of RF clutter is demonstrated in Fig. 4.11, where a CW and two subcarriers of a tag that implements FSK modulation are depicted. In one case (Fig. 4.11-left) the tag operates at 100 and 125 kHz which are close to the frequency of the CW, resulting in a measured bit error rate (BER) of 35%. However, in the other case (Fig. 4.11-right) the tag modulates using 250 and 300 kHz subcarriers which results in a BER of 3.5% (i.e., one order of magnitude less).
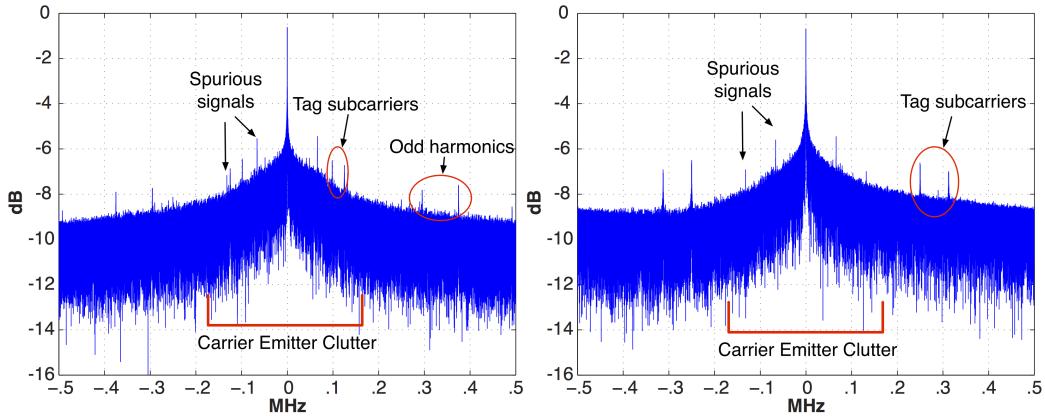
Figure 4.11: Left: tag operating inside RF clutter (BER 35%). Right tag operating away from RF clutter (BER 3.5%)

**Cross Layer Experimentation:** The high level of testbed flexibility facilitates research in areas that require control over all communication layers. Such is the study of the *capture effect*. Specifically, when two nodes utilize the same communication channel, packet collisions may occur. However, under certain conditions, the strongest of the two collided signals can be successfully demodulated, while the other signal is regarded as an attenuated interferer. Although there is theoretical research on the field [51], the study of such scenarios in real systems requires synchronization and control schemes to emulate packet collisions and signal attenuation.

Fig. 4.12-left shows two tags which are forced, through the testbed's remote control, to collide. Both tags are placed close to the reader and are received with comparable power. In this case, information decoding is challenging due to co-channel interference. After OTAP (Fig. 4.12-right), two *distant* tags are forced to collide; the tag closer to the reader is received with a much higher SNR, and thus can be efficiently demodulated. The weakest tag transmission can be seen as noise on top of the strong tag's waveform, exemplifying the capture effect. (i.e. when tag collisions occur) [52].

**Network Layer–Resource Allocation:** Fig. 4.13-left shows the subcarrier frequencies (300, 312 kHz) for a tag that has a measured decoding BER of 3.5 %. A tag with subcarrier frequencies 100 kHz and 125 kHz is then
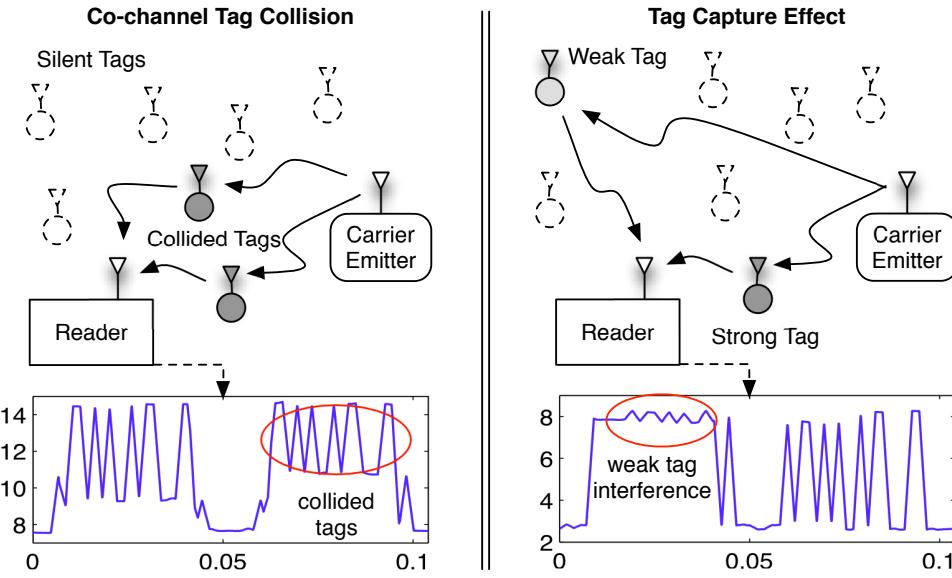
Figure 4.12: Capture effect experimentation. Left: Tags collide by transmitting at the same time. Right: Tags are re-programmed to examine capture effect (strong tag is decoded successfully, even at the presence of a weak interfering tag). The figure depicts real signals captured by the SDR receiver.

activated at the direct vicinity of the reader, Fig. 4.13-right. Due to the fact that the second tag is much closer to the reader, its SNR value is significantly higher than the first one's and the odd harmonics of the second tag overwhelm the subcarriers of the first. This resulted in a significantly worst BER performance of 23 %, while the interfering tag was decoded with a BER of 4.8 %. With utilization of frequency reallocation through the OTAP capability, subcarrier frequencies are reassigned to the tags, thus avoiding interference.
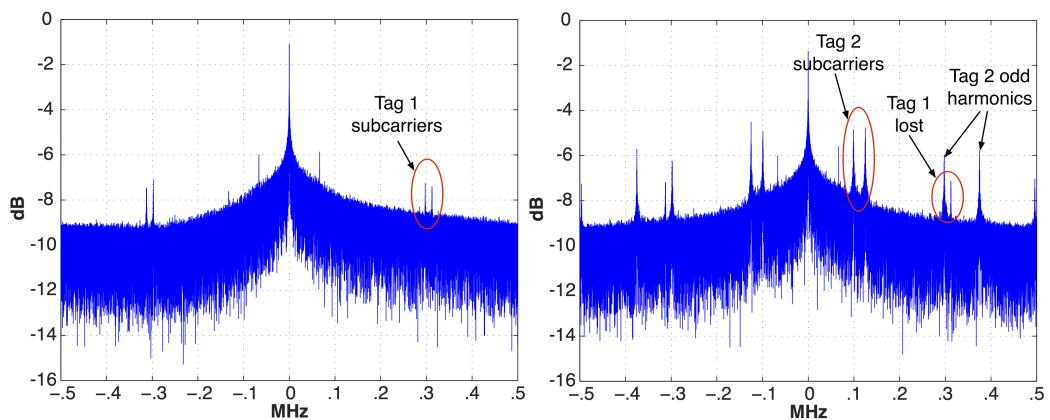
Figure 4.13: Left: Tag 1 operating without interferer with BER 3.5%. Right: Tag 1 operating with BER 35% due to interfering Tag 2 odd harmonics.

# Chapter 5

# Conclusions

## 5.1 Conclusion

This thesis describes in detail the development of a scatter radio network that is composed of low-power and low-cost tags. The tags consist of flexible power supply circuitry, an %RH-to-frequency converter and a sophisticated RF front-end. The communication ranges that were achieved exceeded 130 m with an RMSE of less than 5 %RH, which is a highly promising result for the utilization of the WSN in environmental monitoring applications. The long communication range is due to the utilization of the bistatic topology, FM modulation, battery assisted tags and a sensitive receiver that utilizes smart filtering. For the evaluation of the proposed WSN's performance, a network of 10 tags was fabricated and deployed in a local tomato greenhouse. Finally, for the general context of scatter radio research, a testbed was developed, with OTAP-capable nodes that utilize digital scatter radio communication schemes.

## 5.2 Future Work

This thesis explored the relatively fresh area of scatter radio networking by developing all the components for a solid proof-of-concept communication system. Future efforts should aim to extend the capabilities of the developed system in terms of scale, power and even greater communication range.

Particularly, a network that utilizes numerous CW emitters should be exploited in order to investigate various effects such as the coupling between adjacent cells. Also another issue is the location that each emitter should be installed in order to maximize the coverage of the network.

Moreover, multiple access is an important field that should be thoroughly

researched in order to extend the scale capabilities of this technology. Should the tags be switched on and off in specific time slots in order to exploit time division multiple access? How should the receiver be adjusted in this case?

Most importantly, future work should be focused towards the development of an ultra large-scale (order of 10000) WSN with the proposed architecture. This will require advancements in a lot of theoretical and technical aspects of this work.

# Chapter 6

# Appendix
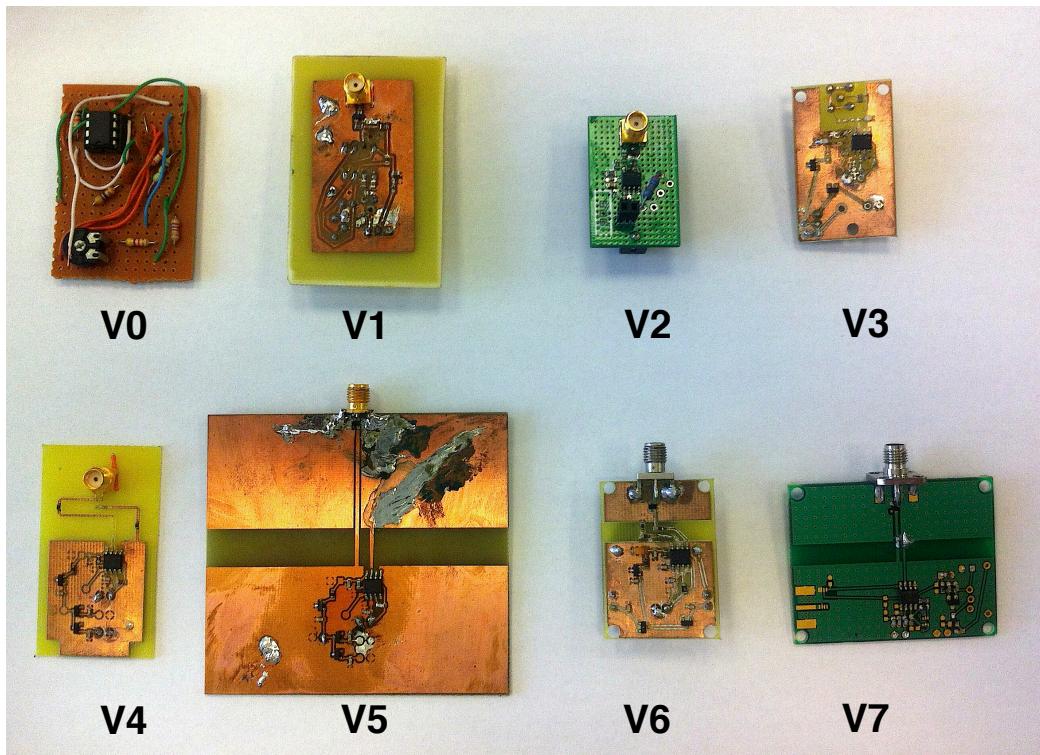


Figure 6.1: The major tag prototypes that were fabricated.
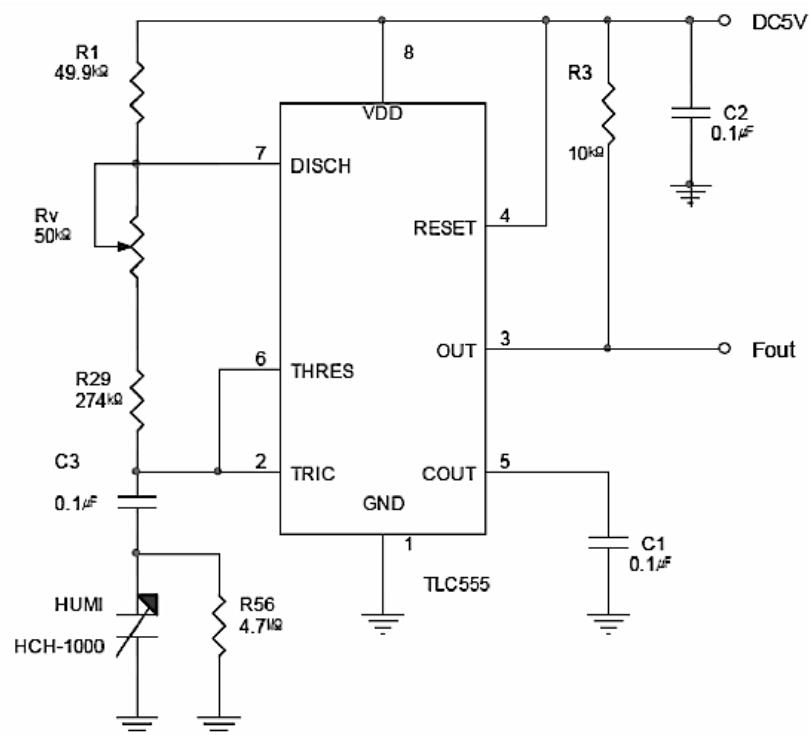
Figure 6.2: V0: Capacitance-to-frequency converter prototype.
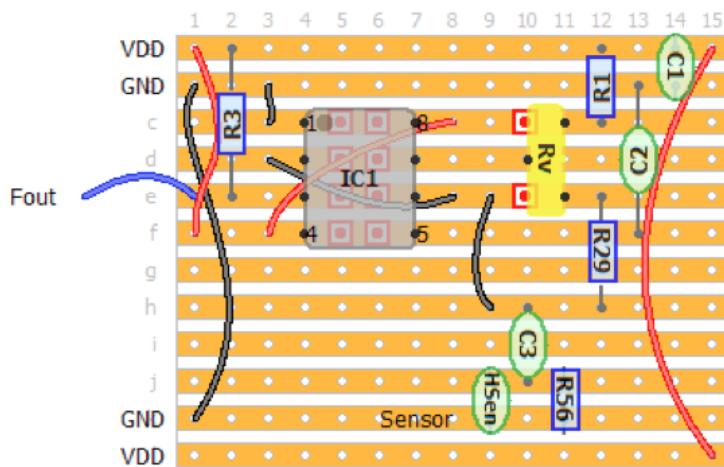


Figure 6.3: V0: Breadboard design of the prototype capacitance-to-frequency converter.
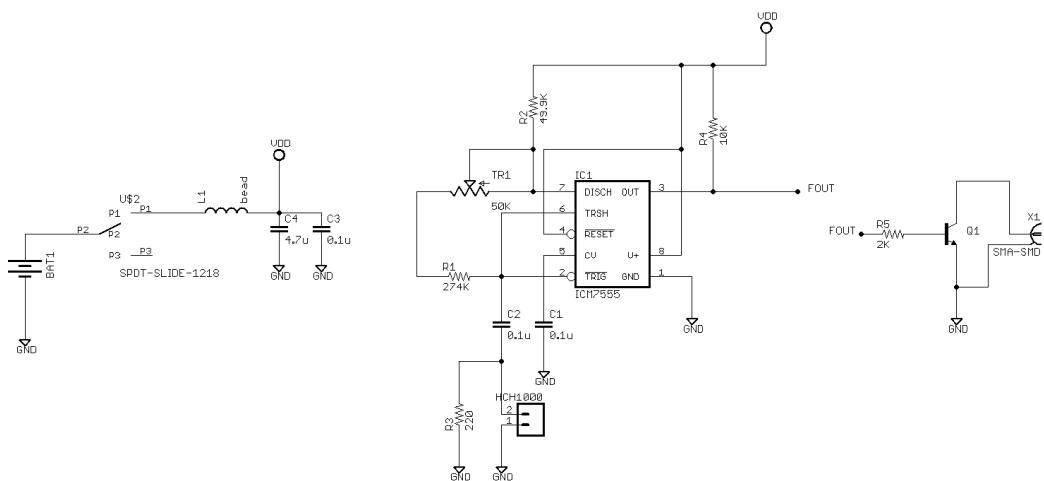
Figure 6.4: Schematic of the first working tag (V1). Utilization of 3V transistor (AT32033), no sophisticated power supply and RF front-end.
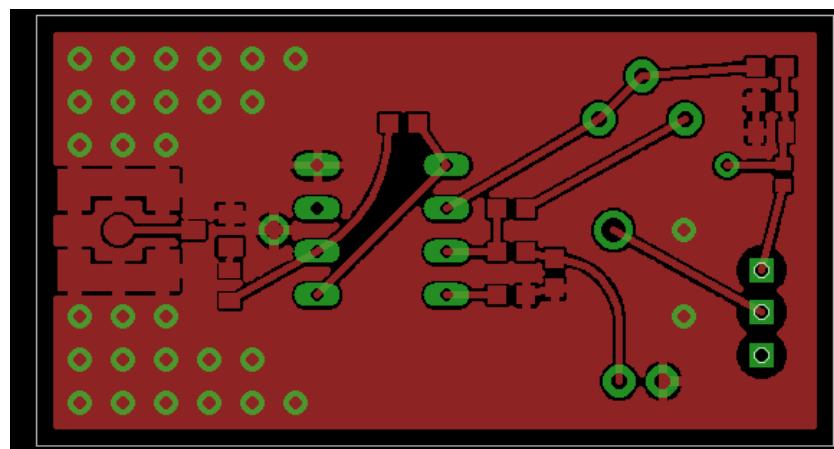


Figure 6.5: Layout of the first scatter radio tag prototype (V1).
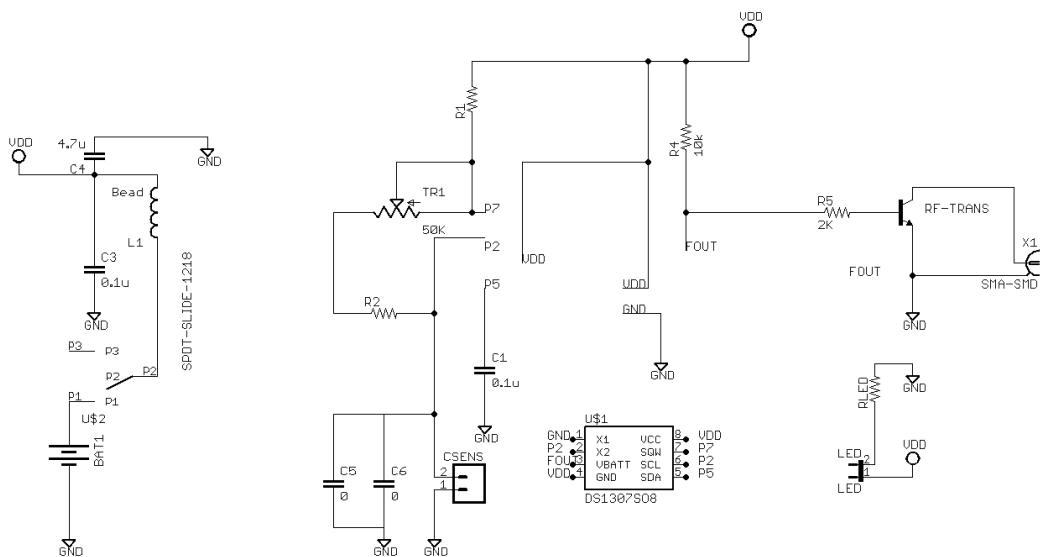
Figure 6.6: V2 schematic. Smaller form factor design, CR2032 battery, SMD 555, ground plane with vias.
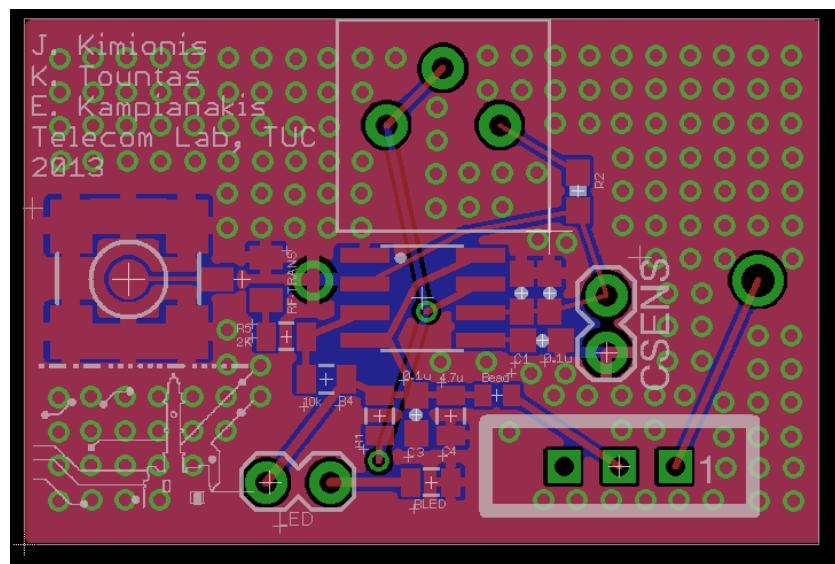


Figure 6.7: V2 layout of the tag.
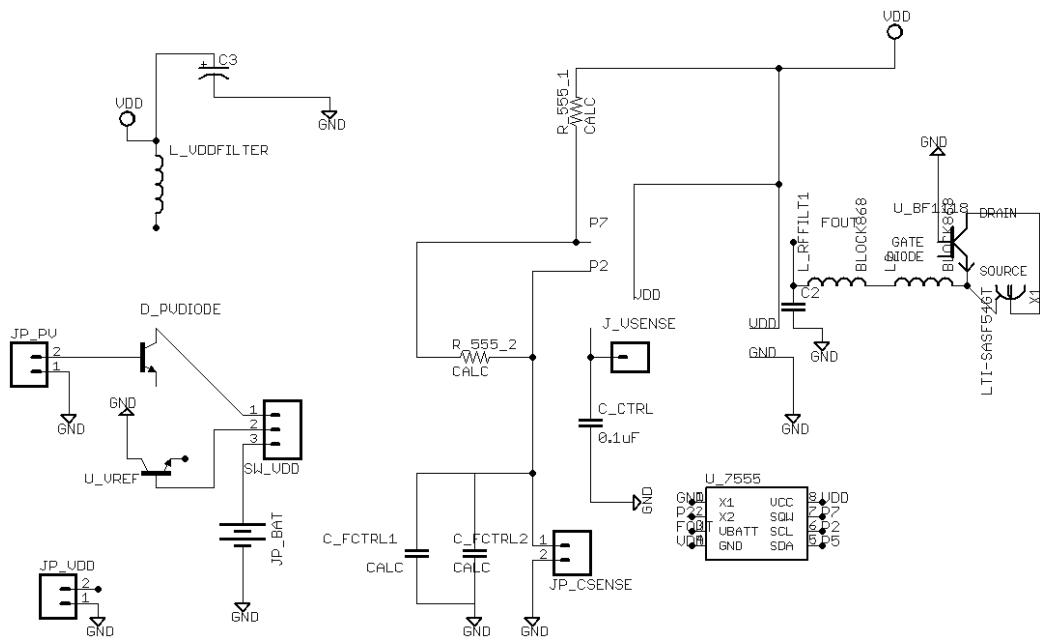
Figure 6.8: V3 schematic. Improved power supply with voltage reference, through-hole SMA (smaller cost), BF1118 utilization, no enhanced RF front-end
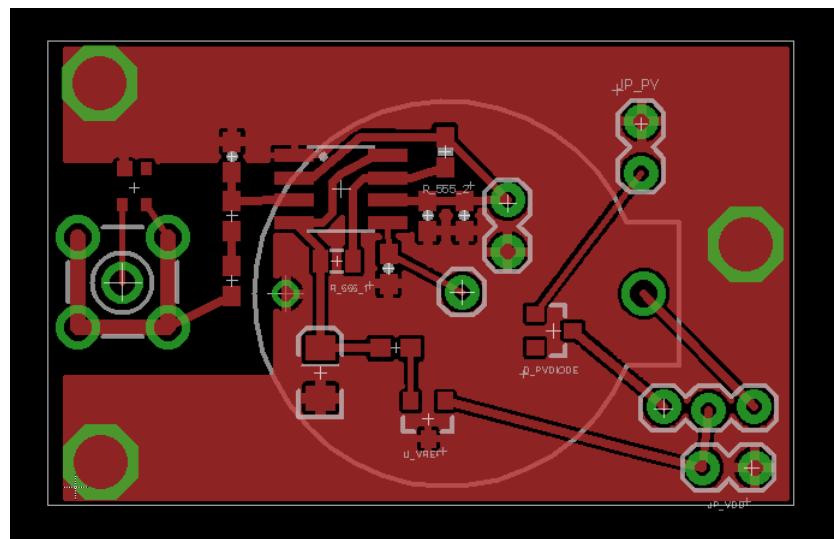


Figure 6.9: V3 layout.
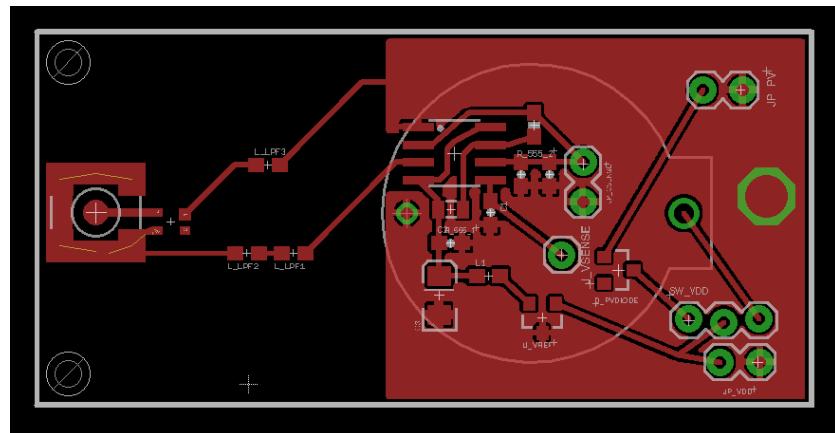
Figure 6.10: V4 layout. First effort for enhanced RF front-end with utilization of chokes. Schematic same as V3.
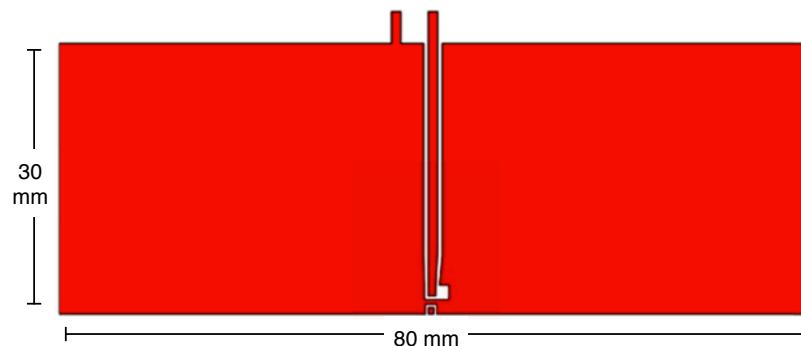


Figure 6.11: Layout of the enhanced RF front-end that is utilized by tag V5. Schematic same as V3.
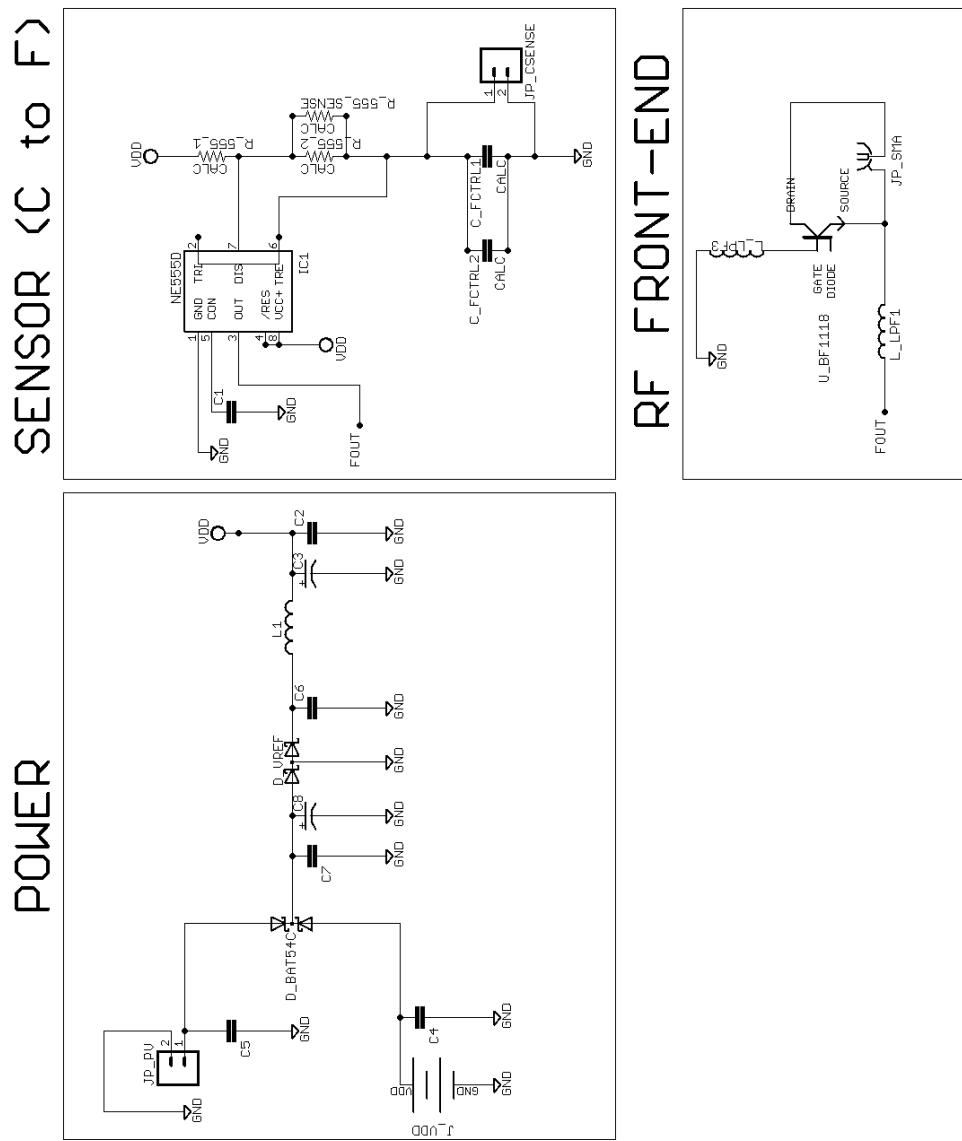
Figure 6.12: V6 Schematic. Utilization of diodes for OR-ing power sources, smaller form factor, straight SMA, stand-off support.
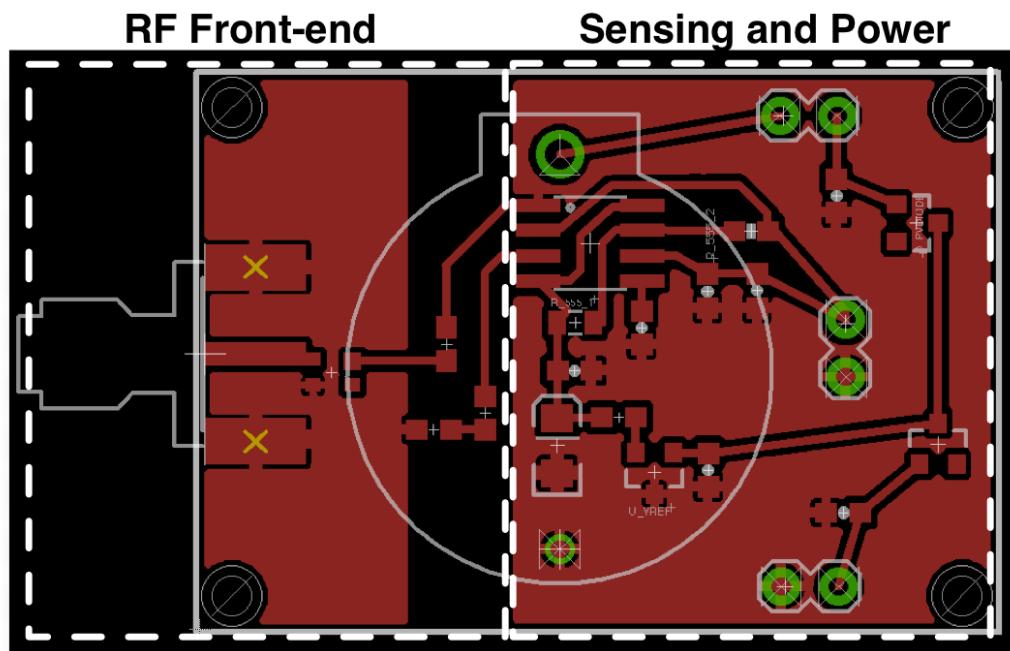
Figure 6.13: V6 layout. Improved for reduced stray capacitances. This is the tag layout that was used in the tomato greenhouse demo.
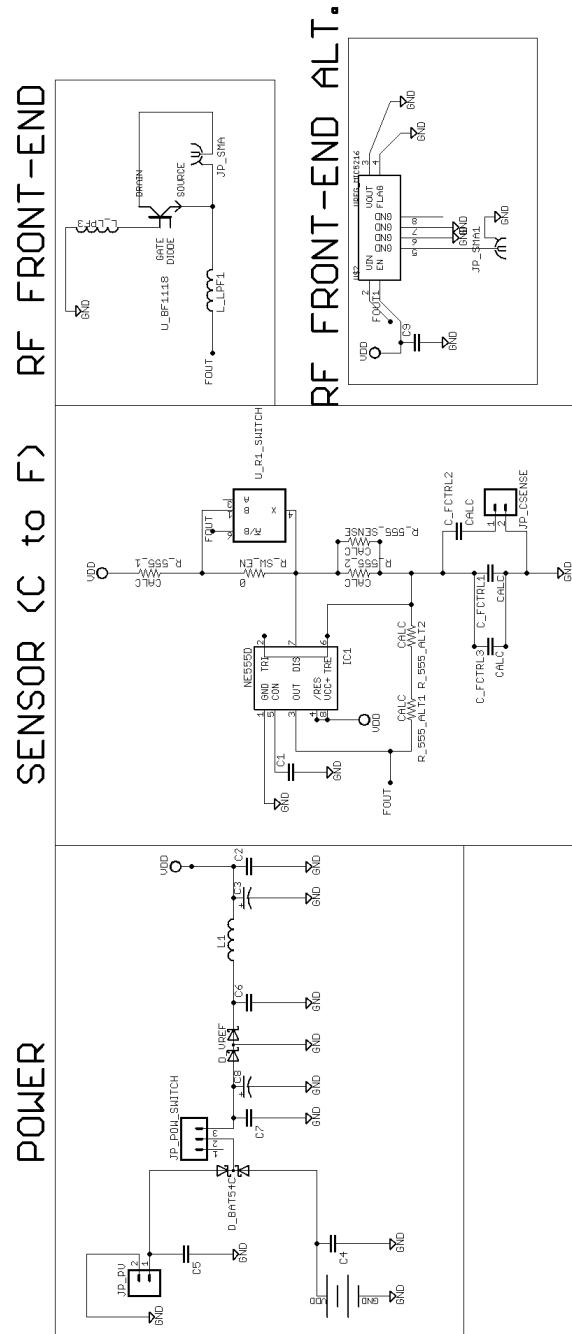
Figure 6.14: V7 schematic. Utilization of two RF front-ends for experimentation with ADG919 switch. Utilization of switch to eliminate current flow from R1 during capacitor discharge, utilization of capacitor in series with sensor, AAA battery and larger RF front-end. Order of 10 less power consumption (100 uW). Not tested in a network deployment, future work.
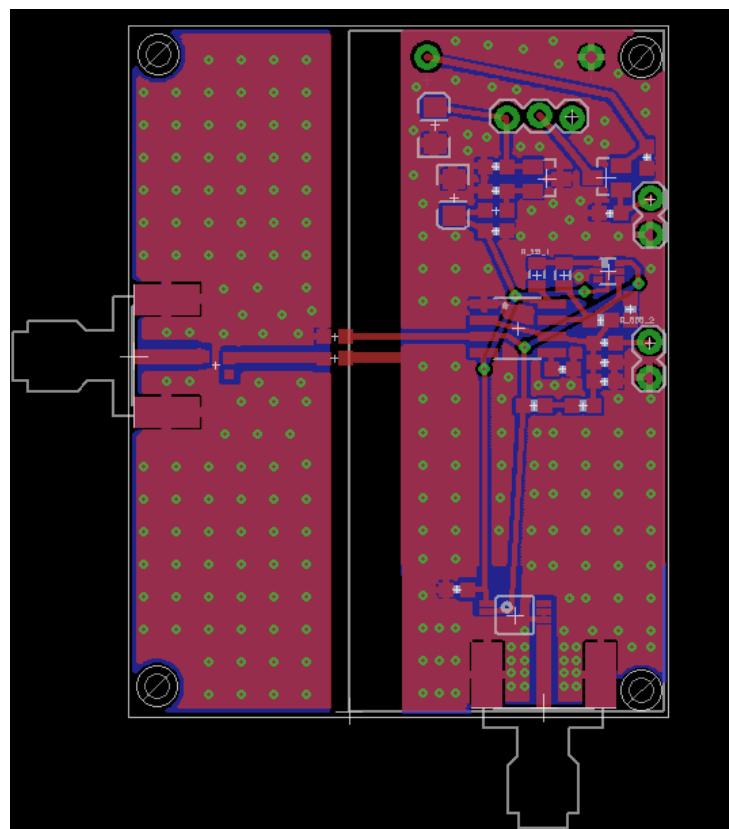
Figure 6.15: V7 layout.

Table 6.1: Tag bill of materials.

| # | Qty. | Schematic ID | Description | Man. ID |
|---|---|---|---|---|
| 1 | 6 | C1,C2,C4,C5,C6,C7 | Cap., 0.1uF, 603, | C0805C104K3RACTU |
| 2 | 2 | C3,C8 | Cap., 1uF, 1206 | C0805C105K8RACTU |
| 3 | 1 | JP_VDD | CR2032 Batt. Holder | BS-7 |
| 4 | 2 | JP_PV,JP_CSENSE | 2x1 DIP Header | SSA-132-S-T |
| 5 | 1 | D_BAT54C | BAT54C Diodes | BAT54C-G3-08 |
| 6 | 1 | D_VREF | Voltage Ref. IC | REF3020AIDBZT |
| 7 | 1 | NE555D | 555 Timer IC | ICM7555IBAZ |
| 8 | 2 | R_5551,R_5552 | Timing Res. | N/A |
| 9 | 2 | C_FCTRL1,C_FCTRL2 | Timing Cap. | N/A |
| 10 | 1 | U_BF1118 | MOSFET RF Switch | BF1118WR,115 |
| 11 | 2 | L_LPF1,L_LPF2 | RF Chokes | BLM18GG471SN1D |
| 12 | 1 | JP_SMA | SMA RF Conn. | 142-0701-806 |

# Bibliography

[1] S. Mini, S. Udgata, and S. Sabat, "Sensor deployment and scheduling for target coverage problem in wireless sensor networks," *IEEE Sensors J.*, vol. 14, no. 3, pp. 636–644, Mar. 2014.

[2] R. Yao, W. Wang, M. Farrokh-Baroughi, H. Wang, and Y. Qian, "Quality-driven energy-neutralized power and relay selection for smart grid wireless multimedia sensor based IoTs," *IEEE Sensors J.*, vol. 13, no. 10, pp. 3637–3644, Oct. 2013.

[3] G. Tolle, J. Polastre, R. Szewczyk, D. Culler, N. Turner, K. Tu, S. Burgess, T. Dawson, P. Buonadonna, D. Gay, and W. Hong, "A macroscope in the redwoods," in *Proc. ACM Embedded Networked Sensor Systems Conf. (SenSys)*, San Diego, CA, Nov. 2005, pp. 51–63.

[4] S. Zhang, G. Tan, H. Jiang, B. Li, and C. Wang, "On the utility of concave nodes in geometric processing of large-scale sensor networks," *IEEE Trans. Wireless Commun.*, vol. 13, no. 1, pp. 132–143, Jan. 2014.

[5] J. Lee and C. Tepedelenlioglu, "Distributed detection in coexisting large-scale sensor networks," *IEEE Sensors J.*, vol. 14, no. 4, pp. 1028–1034, Apr. 2014.

[6] D. Arifler, "Optimality of homogeneous sensing range assignment in large-scale wireless sensor network deployments," *IEEE Commun. Lett.*, vol. 16, no. 9, pp. 1489–1491, Sep. 2012.

[7] G. Shi, J. Zheng, J. Yang, and Z. Zhao, "Double-blind data discovery using double cross for large-scale wireless sensor networks with mobile sinks," *IEEE Trans. Veh. Technol.*, vol. 61, no. 5, pp. 2294–2304, Jun. 2012.

[8] Y. Liu, X. Mao, Y. He, K. Liu, W. Gong, and J. Wang, "Citysee: not only a wireless sensor network," *IEEE Network*, vol. 27, no. 5, pp. 42–47, Sep. 2013.

[9] Y. Liu, Y. He, M. Li, J. Wang, K. Liu, L. Mo, W. Dong, Z. Yang, M. Xi, J. Zhao, and X.-Y. Li, "Does wireless sensor network scale? a measurement study on GreenOrbs," in *Proc. IEEE Int. Conf. on Computer Communications (INFOCOM)*, Shanghai, China, April 2011, pp. 873–881.

[10] L. Mottola and G. P. Picco, "Programming wireless sensor networks: Fundamental concepts and state of the art," *ACM Computing Surveys*, vol. 43, no. 3, pp. 19:1–19:51, Apr. 2011.

[11] H. Stockman, "Communication by means of reflected power," *Proc. IRE*, pp. 1196–1204, Oct. 1948.

[12] S. Thomas and M. Reynolds, "QAM backscatter for passive UHF RFID tags," in *Proc. IEEE RFID Conf.*, Orlando, FL, Apr. 2010, pp. 210–214.

[13] G. Vannucci, A. Bletsas, and D. Leigh, "A software-defined radio system for backscatter sensor networks," *IEEE Trans. Wireless Commun.*, vol. 7, no. 6, pp. 2170–2179, Jun. 2008.

[14] V. Lakafosis, A. Rida, R. Vyas, L. Yang, S. Nikolaou, and M. M. Tentzeris, "Progress towards the first wireless sensor networks consisting of inkjet-printed, paper-based RFID-enabled sensor tags," *Proc. IEEE*, vol. 98, no. 9, pp. 1601–1609, Sep. 2010.

[15] A. Sample, D. Yeager, P. Powledge, and J. Smith, "Design of a passively-powered, programmable sensing platform for UHF RFID systems," in *Proc. IEEE RFID Conf.*, Grapevine, TX, Mar. 2007, pp. 149–156.

[16] D. M. Dobkin, *The RF in RFID: Passive UHF RFID in Practice.*, Newnes (Elsevier), 2008.

[17] U. Karthaus and M. Fischer, "Fully integrated passive uhf RFID transponder ic with 16.7$\mu$w minimum rf input power," *IEEE J. Solid-State Circuits*, pp. 1602–1608, Oct. 2003.

[18] A. Bletsas, A. G. Dimitriou, and J. N. Sahalos, "Improving backscatter radio tag efficiency," *IEEE Trans. Microwave Theory Tech.*, vol. 58, no. 6, pp. 1502–1509, Jun. 2010.

[19] J. Griffin and G. Durgin, "Gains for rf tags using multiple antennas," *IEEE Trans. Antennas Propagat.*, vol. 56, no. 2, pp. 563–570, Feb. 2008.

[20] J. Kimionis, A. Bletsas, and J. N. Sahalos, "Bistatic backscatter radio for tag read-range extension," in *IEEE Int. Conf. on RFID-Technologies and Applications (RFID-TA)*, Nice, France, Nov. 2012, pp. 356–361.

[21] J. Kimionis, A. Bletsas, and J. N. Sahalos, "Design and implementation of RFID systems with software defined radio," in *6th IEEE European Conf. on Antennas and Propagation (EuCAP)*, Prague, Czech Republic, Mar. 2012, pp. 3464–3468.

[22] J. Kimionis, A. Bletsas, and J. N. Sahalos, "Increased range bistatic scatter radio," *IEEE Trans. Commun.*, vol. 62, no. 3, pp. 1091–1104, Mar. 2014.

[23] M. A. Eden, R. A. Hill, R. Beresford, and A. Steward, "The influence of inoculum concentration, relative humidity, and temperature on infection of greenhouse tomatoes by botrytis cinerea." *Plant Pathology*, vol. 45, no. 4, pp. 795–806, Aug. 1996.

[24] L. Mortensen, "Effect of relative humidity on growth and flowering of some greenhouse plants," *Scientia Horticulturae*, vol. 29, no. 4, pp. 301–307, Aug. 1986.

[25] K. Lasanen and J. Kostamovaara, "A 1.2-V CMOS oscillator for capacitive and resistive sensor applications," *IEEE Trans. Instrum. Meas.*, vol. 57, no. 12, pp. 2792–2800, Dec. 2008.

[26] Z. Tan, R. Daamen, A. Humbert, Y. Ponomarev, Y. Chae, and M. Pertijs, "A 1.2-V 8.3-nJ CMOS humidity sensor for RFID applications," *IEEE J. Solid-State Circuits*, vol. 48, no. 10, pp. 2469–2477, Oct. 2013.

[27] A. D. DeHennis and K. D. Wise, "A wireless microsystem for the remote sensing of pressure, temperature, and relative humidity," *J. Microelectromech. Syst.*, vol. 14, no. 1, pp. 12–22, Feb. 2005.

[28] D. Cirmirakis, A. Demosthenous, N. Saeidi, and N. Donaldson, "Humidity-to-frequency sensor in CMOS technology with wireless readout," *IEEE Sensors J.*, vol. 13, no. 3, pp. 900–908, Mar. 2013.

[29] C. Alippi, R. Camplani, C. Galperti, and M. Roveri, "A robust, adaptive, solar-powered WSN framework for aquatic environmental monitoring," *IEEE Sensors J.*, vol. 11, no. 1, pp. 45–55, Jan. 2011.

[30] H.-C. Lin, Y.-C. Kan, and Y.-M. Hong, "The comprehensive gateway model for diverse environmental monitoring upon wireless sensor network," *IEEE Sensors J.*, vol. 11, no. 5, pp. 1293–1303, May 2011.

[31] T. Davis, X. Liang, C.-M. Kuo, and Y. Liang, "Analysis of power characteristics for sap flow, soil moisture, and soil water potential sensors in wireless sensor networking systems," *IEEE Sensors J.*, vol. 12, no. 6, pp. 1933–1945, Jun. 2012.

[32] E. Kampianakis, J. Kimionis, C. Konstantopoulos, E. Koutroulis, and A. Bletsas, "Backscatter sensor network for extended ranges and low cost with frequency modulators: Application on wireless humidity sensing," in *Proc. IEEE Sensors Conf.*, Baltimore, MD, Nov. 2013.

[33] E. Kampianakis, J. Kimionis, C. Konstantopoulos, E. Koutroulis, and A. Bletsas, "Wireless environmental sensor networking with analog scatter radio & timer principles," *IEEE Sensors J.*, submitted for publication.

[34] S. D. Assimonis, E. Kampianakis, and A. Bletsas, "Microwave analysis and experimentation for improved backscatter radio," in *8th IEEE Eu-*

*ropean Conf. on Antennas and Propagation (EuCAP)*, Hague, Netherlands, Apr. 2014.

[35] A. Bletsas, S. Siachalou, and J. N. Sahalos, "Anti-collision backscatter sensor networks," *IEEE Trans. Wireless Commun.*, vol. 8, no. 10, pp. 5018–5029, Oct. 2009.

[36] S. W. Smith, *The scientist and engineer's guide to digital signal processing.*, California Technical Publishing, San Diego, 1997.

[37] J. Fraden, *Handbook of Modern Sensors.*, Springer, 2010.

[38] J. Fan and I. Gijbels, *Local Polynomial Modelling and Its Applications.*, Chapman and Hall/CRC, 1996.

[39] M. Kass and J. Solomon, "Smoothed local histogram filters," *ACM Transactions on Graphics (TOG)*, vol. 29, no. 4, pp. 100–105, 2010.

[40] F. C. Schoute, "What is a Savitzky-Golay filter?," *IEEE Signal Processing Mag.*, vol. 28, no. 4, pp. 111–117, Jul. 2011.

[41] K. Pandia, S. Ravindran, R. Cole, G. Kovacs, and L. Giovangrandi, "Motion artifact cancellation to obtain heart sounds from a single chest-worn accelerometer," in *Proc. IEEE Int. Conf. on Acoustics, Speech, and Signal Processing (ICASSP)*, Dallas, TX, Mar. 2010, pp. 590–593.

[42] A. Savitzky and M. J. Golay, "Smoothing and differentiation of data by simplified least squares procedures." *Analytical chemistry*, vol. 36, no. 8, pp. 1627–1639, Jul. 1964.

[43] *CC2500 2.4GHz RF transceiver, product manual*, 1st ed., Texas Iinstruments, 2009, available online.

[44] E. Kampianakis, J. Kimionis, K. Tountas, and A. Bletsas, "A remotely programmable modular testbed for backscatter sensor network research," in *Proc. 5th Workshop on Real-World Wireless Sensor Networks (REALWSN)*, Como Lake, Italy, Sep. 2013, pp. 153–161.

[45] J. Kimionis, "Design and implementation of backscatter links with soft-ware defined radio for wireless sensor network applications," Diploma Thesis, supervisor Aggelos Bletsas, Technical University of Crete, 2011.

[46] G. Werner-Allen, P. Swieskowski, and M. Welsh, "Motelab: a wireless sensor network testbed," in *Fourth International Symposium on Information Processing in Sensor Networks (IPSN), 2005*, Apr. 2005, pp. 483–488.

[47] J. Griffin, G. Durgin, A. Haldi, and B. Kippelen, "How to construct a test bed for RFID antenna measurements," in *IEEE Antennas and Propagation Society International Symposium 2006*, Jul. 2006, pp. 457–460.

[48] M. Dickens, B. Dunn, and L. J. Nicholas, "Design and implementation of a portable software radio," *IEEE Commun. Mag.*, vol. 46, no. 8, pp. 58–66, Aug. 2008.

[49] A. Bletsas, A. Vlachaki, E. Kampianakis, G. Sklivanitis, J. Kimionis, K. Tountas, M. Asteris, and P. Markopoulos, "Towards precision agriculture: Building a soil wetness multi-hop WSN from first principles," in *Second International Workshop in Sensing Technologies in Architecture, Forestry and Environment (ECOSENSE)*, Belgrade, Serbia, Apr. 2011.

[50] E. Kampianakis, "Custom over the air programmable embedded radios," Diploma Thesis, supervisor Aggelos Bletsas, Technical University of Crete, 2011.

[51] Y.-C. Lai and L.-Y. Hsiao, "General binary tree protocol for coping with the capture effect in RFID tag identification," *IEEE Commun. Lett.*, vol. 14, no. 3, pp. 208–210, Mar. 2010.

[52] A. Bletsas, J. Kimionis, A. G. Dimitriou, and G. N. Karystinos, "Single-antenna coherent detection of collided FM0 RFID signals," *IEEE Trans. Commun.*, vol. 60, no. 3, pp. 756–766, Mar. 2012.